Noise protected two-qubit gate using anisotropic exchange interaction

Master's Thesis

Zizheng Wu

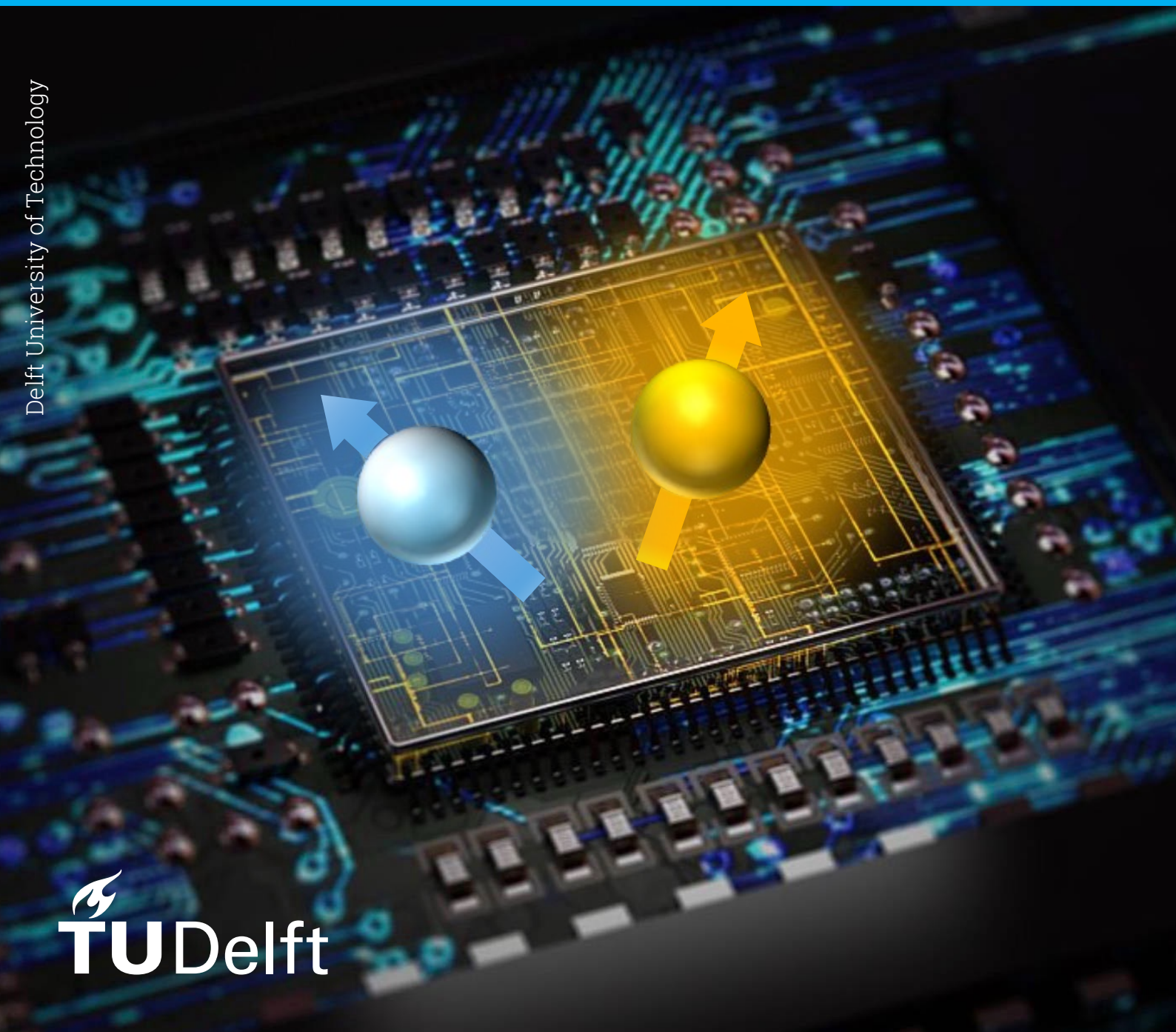

Delft University of Technology

TU Delft

Noise protected two-qubit gate using anisotropic exchange interaction

High fidelity two-qubit gate made by hole spin qubits

by

Zizheng Wu

Supervisor:	Maximilian Rimbach-Russ
Project Duration:	Aug, 2024 - Feb, 2025
Faculty:	Faculty of Applied Sciences, Delft QuTech

Cover: The cover design was inspired by an artistic image on the QuTech website. Credit: Marieke de Lorijn for QuTech. The circuit on the cover is a modified version of the image retrieved from `https://www.sohu.com/a/635128001_121372262`.

Contents

1

Introduction

In 1946, the announcement of ENIAC (Electronic Numerical Integrator and Computer), the first general-purpose digital computer, marked a milestone in the development of computers [1]. Together with the burgeoning of the semiconductor technology, computers gradually transformed from a massive, room-sized machine into a small, sophisticated device with a remarkable increase in the computing efficiency. In 1958, Jack Kilby successfully demonstrated that integrating electronic components onto a single chip was possible [2]. His success unveiled the development of the integrated circuit, which revolutionized the industry and made personal computers accessible to the general public.

This rapid technological evolution in the integrated circuit is guided by an empirical trend, summarized as the Moore's Law. It gives a rough prediction that the number of transistors on a chip would double approximately every two years. However, when the transistors start entering the atomic-scale, physical limitations including quantum tunneling and heat dissipation add much difficulty in keep reducing the chip size [3]. With the growing demand for computational resources from various industries, finding solutions to overcome this challenge has become urgent. Among these, building quantum computers stands out as a promising approach.

To overcome the current challenges faced by classical computers, we need to explore novel computing methods. If the traditional binary-encoded classical computers cannot solve highly complex problems, we can consider adopting a different computing paradigm. Quantum mechanics offers us another choice of encoding information. Instead of using classical bits which can only be in one of the two states 0 or 1, quantum computers use qubits (quantum bits). According to the principles of quantum mechanics, qubits can exist in a superposition state of 0 and 1 simultaneously. When the number of qubits becomes large, this property enables quantum computers to process a vast amount of information in parallel. Additionally, Quantum mechanics also allows qubits to be entangled, meaning the state of one qubit is directly related to the state of another, even if they are spatially separated at a large distance [4]. The two exclusive properties of qubits make quantum computers theoretically much more powerful than classical computers.

The past few decades have witnessed the rapid and prosperous development of quantum computers. Many physical systems have been explored and verified as feasible candidates for qubits, including superconducting qubits [5], trapped ions [6], photons [7] and Rydberg atoms [8]. In 1998, Daniel Loss and David DiVincenzo first proposed that we could use coupled quantum dot systems to perform quantum computation [9]. More specifically, we could confine electrons in quantum dots and use their spin degree of freedom to define a qubit. Researchers have placed high expectations on semiconductor quantum dot spin qubits. They are promising qubit platforms for large-scale quantum computing architecture owing to the nanoscale size of quantum dots. Besides, their compatibility with the well-established semiconductor fabrication technology is a significant advantage [10].

In the past 26 years since the proposal, great achievements have been made in developing quantum computers using silicon-based electron spin qubits. For single qubit manipulation, the fidelity can reach above 99.9% [11] and for two-qubit gate, the gate fidelity can also exceed 99%, which meets the threshold requirement for fault-tolerant quantum computing [12, 13, 14, 15, 16]. Building upon the significant progress made in electron spin qubits, researchers are now exploring the potential of hole spin qubits. In recent years, germanium hole spin qubits have become a research hotspot due to some advantages. Similar to silicon, germanium is also a Group IV semiconductor, which makes it possible to protect hole spins from the influence of nuclear spins through isotopic enrichment [17]. Besides, holes enjoy an absence of valley degeneracy compared with silicon electrons. This eliminates the need for hole spin qubits to address valley splitting which is quite challenging to control over large quantum-dot arrays [18]. So far, germanium hole spin qubits have also achieved high-quality single-qubit gates with fidelity exceeding 99.9% [19]. Two-qubit gate fidelity have reached 99% [20]. Additionally, a two-dimensional 10-qubit array has already been realized by leveraging advanced technique in material growth and semiconductor device fabrication [21].

The most essential property of holes that make it worth studying is their strong spin-orbit interaction. The spin-orbit interaction (also known as the spin-orbit coupling) is a relativistic effect through which the hole's spin can be coupled to its orbital angular momentum [22]. This allows for an efficient all-electric spin manipulation without the need of micromagnets [23, 24]. Another very important feature of the spin-orbit interaction is that it gives rise to the anisotropic exchange interaction. [25, 26, 27]. The exchange interaction is fundamental to the construction of two-qubit quantum gates in semiconductor quantum dot spin qubits. Currently, the modeling, control, and optimization of exchange interaction primarily focus on the isotropic type between electron spins [28, 29]. However, strategies for making full use of the anisotropic exchange interaction — where the interaction strength depends on the direction — between hole spins to implement high-fidelity two-qubit gates remain immature. High-fidelity two-qubit gates are essential for fault-tolerant quantum computing and as hole spin qubits continue to advance, there is an urgent need for a robust strategy to exploit the anisotropic exchange interaction.

Thesis outline

In this thesis, we focus on germanium hole spin qubits and utilize the anisotropic exchange interaction between them to implement two-qubit gates protected against errors by means of composite pulse technique.

Chapter 2 briefly introduces the background knowledge required for this project, including the basics of quantum computing and semiconductor quantum dot spin qubits, hole spin qubits, quantum open system and decoherence.

Chapter 3 gives a concise overview of the composite pulse scheme which is the core technique used throughout this thesis to implement noise-protected two-qubit gates.

In **Chapter 4**, we provide a detailed explanation of how to take advantage of the anisotropic exchange interaction between hole spin qubits and the electric modulation of the g-tensor to implement a composite pulse sequence. This unitary sequence is equivalent to a Controlled-Z(CZ) gate with two single-qubit rotations and it is robust against errors in exchange coupling.

In **Chapter 5**, we design simulations to examine the robustness of the composite pulse scheme. We focus on the performance of multiple gate operations in the presence of quasi-static noise, voltage fluctuation and so on. We will also make a detailed comparison of the composite-pulse scheme with other two-qubit gate protocols: the single-pulse ZZ gate and adiabatic ZZ gate.

In **Chapter 6**, we introduce a powerful mathematical framework: the filter function formalism and use it to analyze the impact of errors caused by time-dependent noise on our composite pulse sequence.

In **Chapter 7**, we summarize the entire thesis and propose some potential future research directions.

2

Background Theory

2.1. Quantum computing and qubits

Quantum computers have the great potential of solving certain specialized tasks exponentially faster than classical computers, which makes them promising for areas such as optimization [30], cryptography [31], and drug discovery [32]. The reason is that quantum computers process information in a fundamentally different way than classical computers.

Classical computers use classical bits as the elementary units of information while quantum information is typically represented in the form of quantum bits (qubits). A classical bit can only be in the state of 0 or 1. For example, it can be implemented by the CMOS technology where bits are represented by two distinct voltage levels: a low voltage for logic 0 and a higher voltage for logic 1 [33]. On the other hand, qubits are quantum two-level systems. In order to describe the quantum properties of qubits, we can for example use tools from linear algebra. Similar to a classical bit, a qubit also has two basis states $|0\rangle$ and $|1\rangle$. But instead of just two binary digits, the two basis states are now vectors in a two-dimensional complex vector space, and they form an orthonormal basis for this $\mathbb{C}^2$, the '$|\rangle$' below is the Dirac notation:

$$|0\rangle = \begin{pmatrix} 1 \\ 0 \end{pmatrix}, |1\rangle = \begin{pmatrix} 0 \\ 1 \end{pmatrix}. \tag{2.1}$$

Here lies the main difference between the classical bits and the qubits. Besides the two states $|0\rangle$ and $|1\rangle$, a qubit can also be in a state which is a linear combination of them:

$$|\psi\rangle = \alpha|0\rangle + \beta|1\rangle, \tag{2.2}$$

where the α and β are complex numbers. This property is called quantum superposition which enables a qubit to contain much more information than a classical bit. According to quantum mechanics, if we do a measurement on this qubit, it will collapse to one of the two basis states, with the probability $|\alpha|^2$ of getting $|0\rangle$ and $|\beta|^2$ of getting $|1\rangle$ respectively. Therefore, $|\alpha|^2 + |\beta|^2 = 1$, since these two states are the only possible outcomes.

Other than the mathematical representation of the state of a qubit, it is also possible to represent its state graphically. Notice the requirement that $|\alpha|^2 + |\beta|^2 = 1$, we can express an arbitrary qubit state as:

$$|\psi\rangle = \cos\frac{\theta}{2}|0\rangle + e^{i\phi}\sin\frac{\theta}{2}|1\rangle. \tag{2.3}$$

The θ and ϕ are similar to the polar angle and azimuthal angle in the spherical coordinates which enables us to correspond the qubit state to a vector starting from the origin and pointing towards the surface of a unit sphere, as shown in the Fig 2.1 below. This method is often referred to as the Bloch sphere representation of the single qubit state.

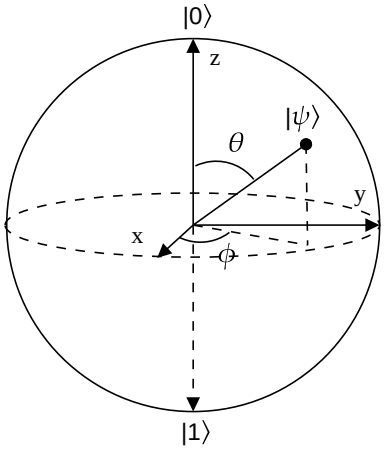

Figure 2.1: The Bloch sphere representation of the qubit state

2.2. Quantum gates

In the previous section, we have introduced that quantum computers encode information into qubits. The next task we should consider is how to make operations on them. In analogy to classical electric circuits which use logic gates such as AND and NOT to act on bits, quantum circuits implement quantum gates on qubits to manipulate the encoded information. In the following paragraphs, we will first introduce single qubit quantum gates and then elaborate on multi-qubit quantum gates.

We have just shown that in the Bloch sphere representation, a single qubit pure quantum state $|\psi\rangle$ can be treated as a unit vector, starting from the origin which is located at the center of the Bloch sphere and ending at a point on the surface of the sphere. A single qubit quantum gate U transforms this $|\psi\rangle$ to another quantum state $|\Psi\rangle = U|\psi\rangle$. Importantly, quantum gates must satisfy the unitary requirement: $U^\dagger U = I$, where $U^\dagger$ is the conjugate transpose of U and I is the identity matrix. This brings about two properties of quantum gates:

- Firstly, all the quantum gates are reversible. If a quantum state undergoes the transform $|\Psi\rangle = U|\psi\rangle$, we can just implement another quantum gate $U^\dagger$ to transform it back to its original state: $U^\dagger|\Psi\rangle = U^\dagger U|\psi\rangle = |\psi\rangle$. This property distinguish

the quantum gates from the classical ones since some of the classical gates are irreversible like the AND gate.

- Secondly, quantum gates preserve the inner product of the quantum states: $\langle\Psi|\Psi\rangle = \langle\psi|U^\dagger U|\psi\rangle = \langle\psi|\psi\rangle$. Therefore, for single qubit quantum gates, the resulting quantum state should also be a unit vector on the Bloch sphere.

The second property implies that single qubit quantum gates are actually implementing rotation operations on the Bloch sphere. As a result, we can write a general expression for single qubit gates:

$$R_{\vec{n}}(\theta) = \exp(-i\theta\vec{n}\cdot\vec{\sigma}/2) = \cos(\frac{\theta}{2})I - i\sin(\frac{\theta}{2})(n_x\sigma_x + n_y\sigma_y + n_z\sigma_z), \tag{2.4}$$

$\vec{n} = (n_x, n_y, n_z)$ is the unit vector indicating the rotation axis, θ is the rotation angle and $\vec{\sigma}$ is the vector $(\sigma_x, \sigma_y, \sigma_z)$ whose components are Pauli matrices. The Fig 2.2 below shows two examples of single qubit quantum gates.

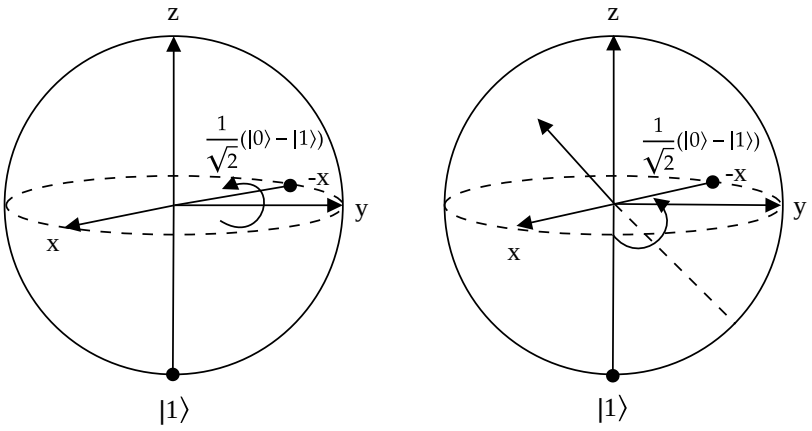

Figure 2.2: Examples of the $R_y(\pi/2)$ gate (left) and the Hadamard gate (right). Both gates rotate $|1\rangle$ to $1/\sqrt{2}(|0\rangle - |1\rangle)$, where the $R_y(\pi/2)$ gate performs a counterclockwise rotation of $\pi/2$ around the y-axis, while the Hadamard gate performs a counterclockwise rotation of π around the direction $\vec{n} = 1/\sqrt{2}(1, 0, 1)$.

Mathematically, quantum gates can be represented by unitary matrices. For instance, the function of a quantum phase gate G_ϕ is to add an additional phase when it is implemented on the $|1\rangle$ state and do nothing if it is implemented on the $|0\rangle$ state: $G_\phi|0\rangle = |0\rangle$, $G_\phi|1\rangle = e^{i\phi}|1\rangle$. We have already seen in Eq 2.1 that $|0\rangle$ and $|1\rangle$ can be written as column vectors. Therefore, this enables us to represent G_ϕ as the following 2×2 matrix:

$$G_\phi = \begin{pmatrix} 1 & 0 \\ 0 & e^{i\phi} \end{pmatrix}. \tag{2.5}$$

For a single qubit, its state space is a 2-dimensional Hilbert space, with basis states $|0\rangle$ and $|1\rangle$ (also known as computational basis states). Suppose now we have a system composed of multiple qubits. What should be its state space? To answer this

question, we can use the concept of tensor product. According to quantum mechanics, if we merge two isolated systems S_1, S_2 into a single one S, the global state space $\mathcal{H}$ is given by the tensor product of $\mathcal{H}_1, \mathcal{H}_2$ which correspond to the individual space of S_1, S_2 [34]:

$$\mathcal{H} = \mathcal{H}_1 \otimes \mathcal{H}_2. \tag{2.6}$$

Consider the case of a two-qubit system. The resulting basis states should be: $\{|0\rangle \otimes |0\rangle, |0\rangle \otimes |1\rangle, |1\rangle \otimes |0\rangle, |1\rangle \otimes |1\rangle\}$, which can be simplified as: $\{|00\rangle, |01\rangle, |10\rangle, |11\rangle\}$. We can see that the dimension of this global system is now $2^2 = 4$. For a system composed of N qubits, its corresponding space dimension should be 2^N. Each of its basis states can be represented by a 2^N-dimensional column vector. Therefore, for a quantum gate acting on N qubits, it can be written mathematically as a $2^N \times 2^N$ matrix.

Two-qubit quantum gates can be broadly categorized into two types: entangling gates, which can generate entangled states, and non-entangling gates which can be constructed using Identity and SWAP gate up to single-qubit operations. The CNOT gate represents an important example of entangling two-qubit gates. Suppose the left qubit is the control qubit and the right one is the target qubit, the CNOT gate flips the target qubit when the control qubit is in the $|1\rangle$ state: $\mathsf{CNOT}|00\rangle = |00\rangle, \mathsf{CNOT}|01\rangle = |01\rangle, \mathsf{CNOT}|10\rangle = |11\rangle, \mathsf{CNOT}|11\rangle = |10\rangle$. Written in matrix, the CNOT gate can be represented as:

$$\mathsf{CNOT} = \begin{pmatrix} 1 & 0 & 0 & 0 \\ 0 & 1 & 0 & 0 \\ 0 & 0 & 0 & 1 \\ 0 & 0 & 1 & 0 \end{pmatrix}. \tag{2.7}$$

Similar to the classical case, any complicated quantum circuit can be constructed using just a simple set of quantum gates. This gate set is called a universal set of quantum gates. One example is that the set of all single-qubit gates and the two-qubit CNOT gate together constitute a universal gate set [35].

2.3. Basics of spin qubits

The DiVincenzo criteria is widely used to exam whether a physical system can function as a viable qubit to make quantum computers [36]. There are five main principles and can be summarized as follows:

- The system should be scalable with well-characterized qubits.
- The qubits can be initialized in a fiducial state. A fiducial state is a standard, well-known initial state or reference state for quantum computations. Normally, we choose the computational basis state $|00...00\rangle$ as the fiducial state, where all qubits are in the $|0\rangle$ state.
- The system's quantum coherence times must be long compared to the gate operation times.

- The system should be capable of implementing a universal gate set including single-qubit gates and two-qubit gates.
- The qubit state can be read out accurately.

Among the many systems that fulfill these requirements, semiconductor quantum dot (QD) spin qubits are promising candidates. The spin degree of freedom of an electron or a hole confined in a gate-defined quantum dot naturally defines a two-level system which enables it to function as a qubit. Furthermore, their compatibility with the well-established semiconductor fabrication technology facilitates the scalability. The two possible spin projection states along a chosen quantization axis (typically the z-axis) are denoted as $|\uparrow\rangle$ and $|\downarrow\rangle$. Based on our discussion in Section 2.1, these states form the computational basis for a qubit, where $|\uparrow\rangle$ can correspond to $|0\rangle$ and $|\downarrow\rangle$ can correspond to $|1\rangle$. The manipulation of spin states is described using the spin operators, which are components of the spin angular momentum vector $\vec{\mathbf{S}} = (S_x, S_y, S_z)$. In the case of a spin-$\frac{1}{2}$ particle, these operators are represented by the Pauli matrices:

$$S_x = \frac{\hbar}{2}\begin{pmatrix} 0 & 1 \\ 1 & 0 \end{pmatrix}, \quad S_y = \frac{\hbar}{2}\begin{pmatrix} 0 & -i \\ i & 0 \end{pmatrix}, \quad S_z = \frac{\hbar}{2}\begin{pmatrix} 1 & 0 \\ 0 & -1 \end{pmatrix}. \tag{2.8}$$

These operators allow the construction of arbitrary spin rotations, which form the basis of single-qubit gate operations as we mentioned in Section 2.2.

Electron spin resonance (ESR) achieves spin rotation by applying an oscillating magnetic field, with the amplitude and phase of the field governing the rotation. However, magnetic control of spin states is typically slow. To overcome this limitation, intrinsic or artificial spin-orbit interactions allows for a electric-to-magnetic signal conversion, thus, giving rise to all-electric control by using electric dipole spin resonance (EDSR) [24]. Qubit readout can be realized through the spin-to-charge conversion [37] or Pauli spin blockade [38]. Following the readout, the exact qubit state is identified. Depending on the outcome, the qubit can either be flipped via a spin manipulation or undergo thermal relaxation, making it initialized to the desired fiducial state for subsequent quantum processes[39].

2.3.1. Exchange interaction

A very fundamental but important concept in spin qubit systems is the exchange interaction which can be classified into direct and kinetic types. Among these, the kinetic exchange interaction is more controllable, making it the preferred choice for spin qubit control. In this subsection, we briefly introduce the physical background behind this kinetic exchange interaction. We limit our discussion to the system in which two electrons occupy two sites. The introduction and formula derivation in this subsection is inspired by [10].

In the simplified Fermi-Hubbard hopping model where we only consider the on-site Coulomb interaction (the energy cost of placing two electrons on the same site) and neglect inter-dot Coulomb interactions and direct exchange terms, the Hamiltonian is given by:

$$H_{\mathrm{FH}} = \sum_{\sigma=\uparrow,\downarrow} \left[\sum_{j=1,2} \mu_j c_{j\sigma}^{\dagger} c_{j\sigma} + t_c \left(c_{1\sigma}^{\dagger} c_{2\sigma} + c_{2\sigma}^{\dagger} c_{1\sigma} \right) \right] + \sum_{j=1,2} U c_{j\uparrow}^{\dagger} c_{j\uparrow} c_{j\downarrow}^{\dagger} c_{j\downarrow}, \tag{2.9}$$

where μ_j represents the electron's potential energy on site j, t_c denotes a constant tunnel coupling between the two sites and U is the on-site Coulomb interaction. Only three configurations are allowed in our system: $(1,1), (2,0), (0,2)$, which correspond to: one electron on each of the two sites, both electrons are localized on site 1 and both electrons are localized on site 2, respectively. According to the Pauli exclusion principle, when both electrons are localized on the same site, they should have the opposite spin direction. Therefore, electrons in the two configurations: $(2,0), (0,2)$ are in the singlet state.

The $(1,1)$ configuration contains four possibilities: one spin-singlet state and three spin-triplet states, depending on the spin direction. We first define: $\mu_1 + \mu_2 = 0$, which makes the eigenenergies of the three spin-triplet states equal to zero. We then define the detuning between the two sites as: $\mu_1 - \mu_2 = \varepsilon$. The Hamiltonian can be rewritten in the following form:

$$\begin{aligned} H = &(U-\varepsilon)|S(0,2)\rangle\langle S(0,2)| + (U+\varepsilon)|S(2,0)\rangle\langle S(2,0)| \\ &+ \sqrt{2}t_c\big(|S(2,0)\rangle\langle S(1,1)| + |S(0,2)\rangle\langle S(1,1)| + h.c.\big). \end{aligned} \tag{2.10}$$

We add another two conditions: the first one is $|t_c| \ll U \pm \epsilon$, which means that the tunnel coupling is weak and we can treat the hopping term using the perturbation theory; the second one is $|\epsilon| < U$, which prevents the system from localizing entirely on one site due to a large detuning. We further write the Hamiltonian as: $H = H_0 + H'$ in which H_0 is the unperturbed Hamiltonian and H' corresponds to the perturbation Hamiltonian. They are given by:

$$H_0 = (U-\varepsilon)|S(0,2)\rangle\langle S(0,2)| + (U+\varepsilon)|S(2,0)\rangle\langle S(2,0)|, \tag{2.11}$$

$$H' = \sqrt{2}t_c\big(|S(2,0)\rangle\langle S(1,1)| + |S(0,2)\rangle\langle S(1,1)| + h.c.\big). \tag{2.12}$$

We treat $|S(1,1)\rangle$ as the unperturbed ground state with energy with $E^{(0)} = 0$ due to $\mu_1 + \mu_2 = 0$. The first-order corrected wavefunction can be expressed as:

$$|S'\rangle = |S(1,1)\rangle + \sum_{n\neq 0} \frac{\langle S_n|H'|S(1,1)\rangle}{E^{(0)} - E_n}|S_n\rangle, \tag{2.13}$$

where $|S_n\rangle$ are the two virtual states $|S(2,0)\rangle, |S(0,2)\rangle$ and E_n are the energies of these two states. The final results of the $|S'\rangle$ is a hybridized singlet state:

$$|S'\rangle = |S(1,1)\rangle - \frac{\sqrt{2}t_c}{U+\epsilon}|S(2,0)\rangle - \frac{\sqrt{2}t_c}{U-\epsilon}|S(0,2)\rangle. \tag{2.14}$$

From the Hamiltonian, we can see that the first-order energy correction is zero, and according to the equation:

$$\Delta E^{(2)} = \sum_{n\neq 0} \frac{|\langle S_n|H'|S(1,1)\rangle|^2}{E_0^{(0)} - E_n^{(0)}}, \tag{2.15}$$

the second-order energy correction is given by:

$$\Delta E_S = -\left(\frac{|\langle S(2,0)|H'|S(1,1)\rangle|^2}{U+\epsilon} + \frac{|\langle S(0,2)|H'|S(1,1)\rangle|^2}{U-\epsilon}\right). \tag{2.16}$$

After simplification, we have:

$$\Delta E_S = -\frac{4Ut_c^2}{U^2-\epsilon^2}. \tag{2.17}$$

In summary, if we assume the condition $|t_c| \ll U \pm \epsilon, |\epsilon| < U$, the virtual hopping(or tunneling) will induce a hybridized singlet state $|S'\rangle$ and lower the energy of the original singlet state $|S(1,1)\rangle$ by $4Ut_c^2/(U^2-\epsilon^2)$. This amount of energy represents the exchange coupling J. Neglecting other states with relatively higher energy, we can arrive at the Hamiltonian: $H = J\vec{S_1}\cdot\vec{S_2}$, where $\vec{S_i}$ represents the the spin operator of the electron at site i. This Hamiltonian is referred to as the Heisenberg exchange Hamiltonian, which is effective in describing the $(1,1)$ configuration system. J is tunable via gate voltage modulation [40] which facilitates the implementation of high-fidelity two-qubit gates [41, 42].

2.4. Hole spin qubits

Fermi energy is a fundamental but important concept in semiconductor materials. It refers to the highest energy level that electrons occupy at absolute zero temperature $T = 0K$. At $T = 0K$, all energy states below the Fermi energy are filled with electrons. Therefore, it is intuitive to see that if the Fermi energy lies below the band gap, a single state in the valence band can become unoccupied. This unoccupied state behaves like a positively charged quasiparticle and it is referred to as a hole. Holes also possess spin states, which can be harnessed as spin qubits. In the following subsections, we will give a brief introduction to hole spin qubits. The topics included are: hole's properties which are different from its electron counterpart, the physics of holes in germanium, and the anisotropy induced by spin-orbit interaction.

2.4.1. Properties of holes

Compared with electrons, holes have a different hyperfine interaction mechanism. The main contribution to the electron's states is the s-orbitals. As demonstrated in

Fig 2.3, this s-like state results in a large overlap of the wavefunction between the electron and the nuclei. This leads to in a type of isotropic Fermi contact hyperfine interaction. From Fig 2.3 we can also see that this wavefunction overlap is small for holes, which makes the contact hyperfine interaction well-suppressed. This is because the hole state is mainly composed of the p-orbitals from the valence bands.

However, this doesn't mean holes do not suffer from the hyperfine interaction. Instead, they experience a different form of hyperfine interaction which is referred to as dipole-dipole hyperfine interaction. This interaction becomes anisotropic, which means the interaction strength can vary based on different directions. For a SiGe/Ge system with a [001] growth direction, this hyperfine interaction is stronger along this direction and weaker in the other two orthogonal directions.

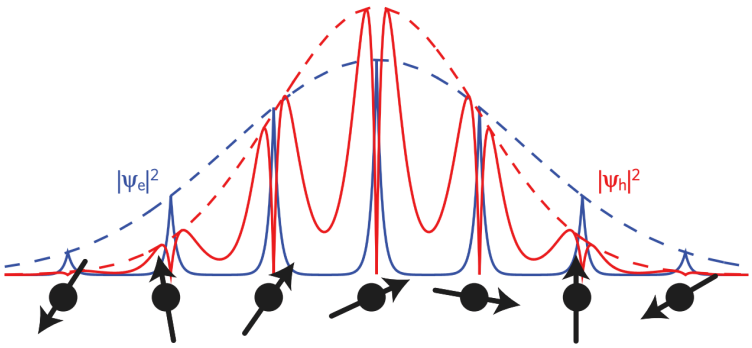

Figure 2.3: Schematic of the electron and hole states. [43]

Secondly, because of holes' strong spin-orbit interaction, spins can be coupled to electric fields which enables all-electric spin manipulation through electric dipole spin resonance (EDSR) technology [23]. However, this strong spin-orbit interaction gives rise to an anisotropic g-tensor and exchange interaction which is quite different from the isotropic Heisenberg exchange interaction of electrons. In later chapters, we will see how this anisotropic exchange interaction can be utilized to construct two-qubit gates.

2.4.2. The physics of holes in germanium

Germanium is emerging as a promising platform for hosting hole spin qubits. In the following paragraphs, we start from introducing the physics of the band structure of bulk germanium, explaining some important concepts such as the heavy-hole and light-hole states. After that, we will move on to the 2-dimensional structure to see how the confinement and strain further affect the band structure.

As mentioned in Subsection 2.4.1, holes reside on the valence band which gives them p-type orbitals with the azimuthal quantum number $l = 1$. This corresponds to a three-fold degeneracy since the magnetic quantum number m_l can take values from $-1, 0, +1$. Together with the spin quantum number $s = 1/2$ which corresponds to $m_s = -1/2, +1/2$, we would expect a six-fold degeneracy at the valence band top.

In fact, the six-fold degeneracy is lifted into two groups: a four-fold and another two-fold degenerate state around the zero crystal momentum region ($\hbar\mathbf{k} = 0$) due to

the spin-orbit interaction. The Hamiltonian that characterizes this interaction can be written as [44]:

$$H_{\text{so}} = \xi_{\text{so}} \mathbf{l} \cdot \mathbf{s}. \tag{2.18}$$

The constant ξ_{so} is the spin-orbit coupling strength and $\mathbf{l}, \mathbf{s}$ corresponds to the orbital and spin angular momentum respectively. The eigenstates of this Hamiltonian are now characterized by the total angular momentum $\mathbf{j} = \mathbf{l} + \mathbf{s}$ and its z-component quantum number m_j. The basic principles of quantum mechanics require that the total quantum number j needs to be integer values and have to satisfy the triangular condition: $|l-s| \leq j \leq l+s$ [45]. For the $l = 1, s = 1/2$ case, j can take values: $3/2, 1/2$ which corresponds to two eigenenergies: $\xi_{so}/2, -\xi_{so}$ (detailed derivation is given in A.2). For $j = 3/2$, m_j can take four values: $3/2, 1/2, -1/2, -3/2$, and therefore it is a four-fold degeneracy while for $j = 1/2$, it is a two-fold degeneracy with m_j can choose between $1/2, -1/2$. The energy gap between these two bands is $\Delta_0 = 3\xi_s o/2$. The $j = 1/2$ band which has a higher energy value is referred to as the split-off band [44].

The properties of the $j = 3/2$ band that is located near the top of the valence band can be derived from the well-known Luttinger-Kohn Hamiltonian [44, 46]. In short, the four degenerate states can be separated into two groups: the heavy-hole band with $m_j = 3/2$ and the light-hole band with $m_j = 1/2$. The 'heavy' and 'light' correspond to the effective mass and this difference leads to the result that the heavy-hole band is higher in energy when the crystal momentum is non-zero.

As mentioned in the first section, a qubit should be a quantum two-level system, with its two energy levels well-isolated from other states to minimize leakage and ensure reliable operation. For holes in germanium, this can for example be realized by moving into a planar heterostructure, in which an external potential is added as a confinement. In this Ge/SiGe heterostructure, there are three important properties:

- At the Ge/SiGe interface, the valence band energy offset traps holes in the Ge quantum well layer [44].
- The in-plane confinement is much weaker than the out-of-plane confinement, making it a quasi-2D system. The holes can move freely in the x-y plane while its coordinate change in the z-axis is strongly limited. The dominance of k_z makes the system eigenstates closely resemble the bulk heavy-hole and light-hole states, which are characterized by their J_z quantum numbers. It also lifts the four-fold degeneracy, resulting in the formation of distinct subbands and a splitting between the heavy-hole-like and light-hole-like states [46].
- The lattice mismatch between the Ge layer and the SiGe layer causes a lateral compressive strain in the quantum well. This strain further splits the heavy-hole and light-hole bands [46].

The Fig 2.4 below provides an illustration of the valence band states for the germanium structures introduced before. The curvature of the energy curve changes for the heavy-hole-like and light-hole-like states of the 2D Ge and Ge/SiGe heterostructure because the in-plane effective mass of light-hole-like bands becomes larger than

the heavy-hole-like bands [46].

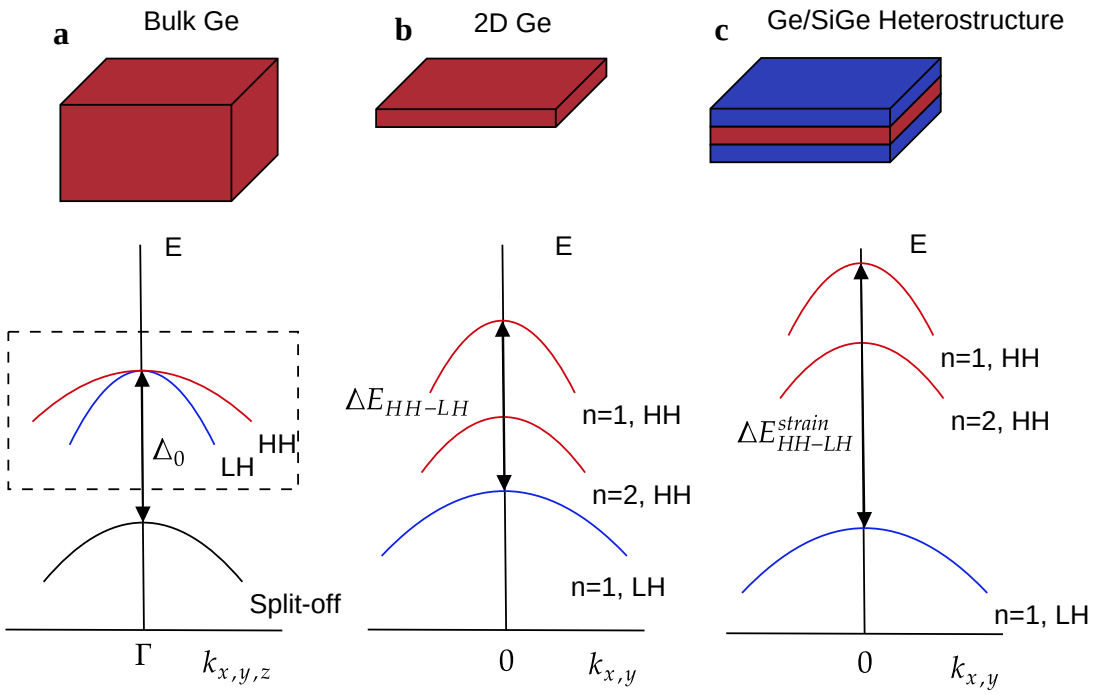

Figure 2.4: Valence band states for different germanium structures: (a) bulk germanium, (b) 2D germanium, (c) Ge/SiGe heterostructure.

2.4.3. The anisotropy

In this section, we briefly introduce how the spin-orbit interaction induce the anisotropic g-tensor and exchange interaction for hole spin qubits. The derivation and discussion of this section is inspired by [18, 46, 47, 48]. As an ansatz, we start from the Luttinger-Kohn Hamiltonian [18]:

$$H_{\mathrm{LK}}(\mathbf{k}) = -\left(\gamma_1 + \frac{5}{2}\gamma_2\right)\frac{\hbar^2 k^2}{2m_0} + \frac{\gamma_2\hbar^2}{m_0}\left(\mathbf{k}\cdot\mathbf{J}\right)^2 + \frac{\gamma_3\hbar^2}{2m_0}\left(\{k_x,k_y\}\{J_x,J_y\} + c.p.\right), \quad (2.19)$$

where $\hbar\mathbf{J}$ denotes spin-$3/2$ operators, γ_1, γ_2, and γ_3 are the Luttinger parameters, m_0 is the bare electron mass, $\{A,B\} = (AB+BA)/2$, and $c.p.$ means cyclic permutations of x, y, z. This Luttinger-Kohn Hamiltonian is widely used to study the topmost valence band states of germanium. From this Hamiltonian, we can recognize a close connection between the $\mathbf{k}$ and $\mathbf{J}$ which arises from the spin-orbit coupling.

The Hamiltonian under the envelop function approximation is given by:

$$H_{\mathrm{env}} = -H_L\left(\frac{\boldsymbol{\pi}}{\hbar}\right) + eV(\mathbf{r}) + 2\kappa\mu_B\mathbf{J}\cdot\mathbf{B} + 2q\mu_B\mathcal{J}\cdot\mathbf{B}, \quad (2.20)$$

where $eV(\mathbf{r})$ is the confining potential applied, κ and q are also the Luttinger parameters, $\mathcal{J} = (J_x^3, J_y^3, J_z^3)$ and $\mathbf{B}$ is the magnetic field. In the presence of external magnetic field, we need to consider the its effect on the electronic state, which is included in the below substitution:

$$\mathbf{B} = \nabla \times \mathbf{A}(\mathbf{r}), \quad \hbar\mathbf{k} \to \boldsymbol{\pi} = -i\hbar\nabla + e\mathbf{A}(\mathbf{r}). \tag{2.21}$$

Based on the Eq 2.20, we apply time inversion to this Hamiltonian and then we can obtain the Zeeman Hamiltonian for holes:

$$H_Z = -2\kappa\mu_B \mathbf{J}\cdot\mathbf{B} - 2q\mu_B \mathcal{J}\cdot\mathbf{B}. \tag{2.22}$$

Projecting the Zeeman Hamiltonian to pure heavy-hole subspaces, we can have the reduced effective Zeeman Hamiltonian:

$$H_{\text{eff},Z} = -\left(3\kappa + \frac{27}{4}q\right)\mu_B B_z \sigma_z - \frac{3}{2}q\mu_B\left(B_x\sigma_x - B_y\sigma_y\right). \tag{2.23}$$

The anisotropy of the g-tensor arises from the fact that $|\kappa| \gg |q|$. Writing the Hamiltonian into a diagonal matrix: diag$(3q, -3q, 6\kappa{+}27q/2)$, we can see a much larger Zeeman splitting in one direction compared with the other two. Further considering the mixture of heavy-hole and light-hole states, we can use the tools from perturbation theory, for example the Schrieffer-Wolff transformation, to add higher-order correction terms to components of the g-tensor [47, 48]. The correction terms are related to the in-plane component of the groundstate wavefunction, which can be tuned by the potential applied. That's the main reason why the g-tensor can be electrically modulated and we will use this property in later chapters.

The spin-orbit interaction will also lead to the anisotropy of the exchange coupling interaction. According to [27], the resulting anisotropic exchange interaction can be described by a rotation matrix which is related to the spin-orbit interaction, the spin-orbit length and the interdot distance. This can also be seen from the fact that there exists a spin rotation angle when the hole performs a tunneling between the quantum dots.

2.5. Quantum open system and decoherence

Most quantum mechanics textbooks introduce the unitary time evolution operator in the beginning chapters, which describes the time evolution of a quantum state governed by the Schrödinger equation. Accordingly, we can predict the state at a future time uniquely by solving the partial derivative equation if we have the Hamiltonian and the initial state. However, unitary time evolution can only describe the dynamics of a closed quantum system which does not interact with the external environment. In reality, closed quantum systems do not exist. Quantum systems will inevitably be coupled to the environment, leading to the transfer of energy between the system and the environment and the loss of phase information. These two processes are referred to

as relaxation and decoherence respectively and these systems are called quantum open systems [49].

When taking the influence of the environment into account, the total Hamiltonian can be written as [50]:

$$H_{\text{tot}} = H_{\text{sys}} + H_{\text{E}} + H_{\text{SE}}. \tag{2.24}$$

where the H_{sys} and H_{E} denotes the system and environment Hamiltonian and H_{SE} denotes the coupling between the system and the environment. In this thesis project, we assume a classical environment, which makes $H_{\text{E}} = 0$. This is because a classical environment typically affects the system through classical external fields, which do not possess quantum degrees of freedom.

To incorporate the effect of the environment, the role of H_{SE} can be understood as introducing corrections to specific parameters in H_{sys}. For a single noisy process and only considering the error's lowest order, this general form can be reduced to:

$$H_{\text{sys}}(1 + \epsilon), \tag{2.25}$$

where ϵ reflects the relative change in the control parameter induced by the environment.

This type of coupling effect is very common in systems such as multispin control in nuclear magnetic resonance or semiconductor quantum dot spin qubits. These systems are highly susceptible to environmental noise or imperfections in control pulses. In this thesis, we focus on the simplest scenario, where the Hamiltonian can be expressed in the form of Eq 2.25. Additionally, we assume that the error term remains constant over a specific timescale, for example, during a single gate operation. This type of error is referred to as systematic error [51].

3

Composite Pulse Technique

3.1. Introduction

Fault-tolerant quantum computing requires that the error rates of quantum gates need to fall below a certain threshold [52]. Therefore, strategies for high-precision quantum control play an important role in the advancement of quantum computers based on semiconductor quantum dot spin qubits. After decades of development, Nuclear Magnetic Resonance (NMR) technology has become highly advanced in the coherent control of nuclear spins dynamics. There are many similarities shared between nuclear spins and electron/hole spins, particularly in their manipulation under external fields. Therefore, some of the well-established pulse techniques developed in NMR provide valuable insights into achieving robust control of electron and hole spins. The construction of using composite pulse sequences is one of them.

The composite pulse technique aims at correcting systematic errors that appear in pulses applied. The core idea of this technique is to substitute a single pulse with a sequence of pulses that implement the same operation. The gained redundancy of the longer gate sequence can then be used to implement operations with a great tolerance. For NMR, there are three dominant systematic errors, namely the under- and over-rotation error (also referred to as pulse length errors), the RF phase error, and the off-resonance error. [51, 53, 54]. For an accurate single qubit gate $R_{\vec{n}}(\theta) = \exp(-i\theta\vec{n}\cdot\vec{\sigma}/2)$ as Eq 2.4 implies, these three types of errors correspond to deviations in θ and $\vec{n}$.

- The under- and over-rotation error can be viewed as a linear shift in the rotation angle. The resulting operator would be:

$$R'_{\vec{n}}(\theta) = \exp(-i(1+\epsilon)\theta\vec{n}\cdot\vec{\sigma}/2). \tag{3.1}$$

  The ϵ is also referred to as the fractional error [51]. For example, if $\epsilon = 0.1$, the pulse will over-rotate 10% of the desired angle.

- For the RF phase error, the error takes place on the $\vec{n}$ which deviates from the original direction. For example, if the resulting $\vec{n}'$ takes the form: $(n_x\cos\epsilon +$

$n_y \sin\epsilon, n_y \cos\epsilon - n_x \sin\epsilon, n_z)$, this means that $\vec{n}$ rotates around the z axis clockwisely by an angle ϵ.

- The off-resonance error occurs due to the mismatch between the driving field frequency and the spin's resonance frequency. The operator becomes:

$$R'_{\vec{n}}(\theta) = \exp(-i\theta(\vec{n}\cdot\vec{\sigma} + \Delta\sigma_z)/2). \tag{3.2}$$

Δ denotes the detuning strength and the $\Delta\sigma_z$ describes the additional phase evolution caused by detuning.

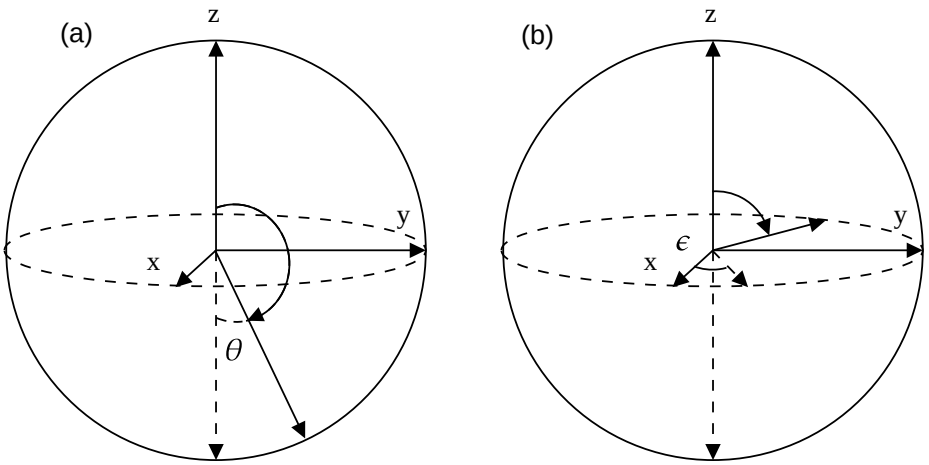

Figure 3.1: Sketch of (a) under-rotation error and (b) RF phase error. For both cases, the initial direction of the spin is along $+z$. For case (a), the ideal rotation is a π rotation around the $+x$ axis, but the actual rotation is $\pi - \theta$, resulting in an incomplete rotation. For case (b), the ideal rotation axis is along $+x$ with a rotation angle of $\pi/2$. However, the rotation axis deviates by an angle ϵ, leading to the final spin deviating from the intended target position.

Fig 3.1 shows examples of under-rotation error and RF phase error. The off-resonance error can be seen as a combination of under/over rotation error and axis deviation error. For quantum gates made by semiconductor quantum dot spin qubits, these three types of errors are also the primary sources of gate infidelity. For example, similar to NMR, random fluctuations or calibration errors in the amplitude or frequency of signals used to control spin qubits, such as microwave or rf pulses, will also cause the under/over rotation or RF phase error [54]. Besides, voltage fluctuations induced by charge noise will affect the hole's g-tensor and result in the fluctuation of Zeeman energy. This will induce off-resonance error, which is also referred to as phase errors. The existence of these error sources highlights the need for advanced error mitigation protocols, such as composite pulse schemes and dynamical decoupling sequences, to achieve reliable and high-fidelity quantum computation.

3.2. The robustness condition

In this section, we give a brief introduction to a key concept in the composite pulse technique, known as the robustness condition. As described in [53, 55], this robustness condition serves as the guiding method for designing the composite pulse sequence to mitigate errors. We assume the elementary pulses that constitute the gate sequence to be:

$$S(\theta, \phi) = \exp[-i\theta(\cos\phi\sigma_x + \sin\phi\sigma_y)/2], \tag{3.3}$$

$$T(\Phi) = \exp[-i\Phi\sigma_z \otimes \sigma_z]. \tag{3.4}$$

According to Section 2.2, $S(\theta, \phi)$ represents a single qubit gate where the rotation axis lies within the xy-plane of the Bloch sphere, θ corresponds to the rotation angle and ϕ defines the orientation of the rotation axis, indicating the angle between the axis and the positive x direction. The two-qubit gate $T(\Phi)$ represents a controlled-phase gate.

Suppose now we want to design a pulse sequence robust against the under- and over-rotation errors. The actual single qubit gate takes the following form:

$$S'(\theta, \phi) = \exp[-i(1+\epsilon)\theta(\cos\phi\sigma_x + \sin\phi\sigma_y)/2]. \tag{3.5}$$

If the deviation angle is relatively small ($|\epsilon| \ll 1$), the fractional error ϵ can be viewed as a perturbation which enables us to expand the $S'(\theta, \phi)$ as:

$$S'(\theta, \phi) = S(\theta, \phi) - i\epsilon\delta S + O(\epsilon^2). \tag{3.6}$$

When constructing a pulse sequence using multiple $S'(\theta, \phi)$ and assuming the error to be systematic, the resulting operator U' would be:

$$U' = S'(\theta_1, \phi_1)S'(\theta_2, \phi_2)...S'(\theta_n, \phi_n). \tag{3.7}$$

We can further rewrite the U' by expanding all the individual pulses like Eq 3.6 and this gives us:

$$U' = U - i\epsilon\delta U + O(\epsilon^2), \tag{3.8}$$

where U is the ideal operator whose components are all error-free:

$$U = S(\theta_1, \phi_1)S(\theta_2, \phi_2)...S(\theta_n, \phi_n). \tag{3.9}$$

So if we deliberately design the pulse sequence such that the $\delta U = 0$, we can have an operator U' that is robust against error in the rotation angle up to the first order.

For example, now consider the pulse sequence [51]:

$$S'(\pi,\pi/3)S'(\pi,5\pi/3)S'(\pi,\pi/3), \tag{3.10}$$

where the elementary pulses within the sequence contain the under- and over-rotation errors: $\theta(1+\epsilon)$. The matrix form of 3.10 is given by:

$$\begin{pmatrix} \cos^3\left(\frac{1}{2}\pi(1+\epsilon)\right) & \frac{1}{4}\cos\left(\frac{\pi\epsilon}{2}\right)\left(-5i+\sqrt{3}+(i+\sqrt{3})\cos(\pi\epsilon)\right) \\ \frac{1}{4}\cos\left(\frac{\pi\epsilon}{2}\right)\left(-5i+\sqrt{3}-(-i+\sqrt{3})\cos(\pi\epsilon)\right) & \cos^3\left(\frac{1}{2}\pi(1+\epsilon)\right) \end{pmatrix}.$$

If we further expand the matrix elements in the error ϵ, we can arrive at the following simplified version:

$$\begin{pmatrix} o^3(\epsilon) & -i+o^2(\epsilon) \\ -i+o^2(\epsilon) & o^3(\epsilon) \end{pmatrix}.$$

From this matrix, we can see that the composite pulse sequence 3.10 approximates a single-qubit X gate up to a global phase. We find that the error in all the matrix elements are at least in the second order, which means that the first-order error is canceled.

The robustness condition can also guide the design of two-qubit gates protected again systematic errors. Here, we assume that the primary noise source originates from the phase term of the ZZ operator $T'(\Phi)=\exp[-i(1+\epsilon)\Phi\sigma_z\otimes\sigma_z]$, while the single-qubit gates in the sequence are assumed to be error-free. Consider the following composite pulses:

$$U' = T'_n(S^1_{n-1}\otimes S^2_{n-1})T'_{n-1}(S^1_{n-2}\otimes S^2_{n-2})...(S^1_1\otimes S^2_1)T'_1. \tag{3.11}$$

Let us expand the $T'(\Phi)$ to first order in error: $(1-i\epsilon\Phi\sigma_z\otimes\sigma_z)T$. Substituting it into Eq 3.11 and writing the resulting unitary operator in the form of Eq 3.8, we obtain the expression for δU. Solving the equation $\delta U=0$ yields the required parameters that can help us build a composite pulse sequence robust against the error in the coupling constant up to first order.

3.3. Two types of composite pulses

In this section, we introduce two composite pulse sequences: SCROFULOUS and Broadband1 (BB1). We will focus on SCROFULOUS, as it plays an important role in this thesis project. In later chapters, we will implement this composite pulse sequence by using hole spin qubits to realize a noise-protected two-qubit gate. In the final part of this section, we provide a brief introduction to BB1.

3.3.1. SCROFULOUS

SCROFULOUS, which stands for 'short composite rotation for undoing length over- and undershoot' [56], is a robust pulse sequence aiming at mitigating systematic errors associated with rotation angles. Consider the case in which we want to apply an ideal single-qubit rotation around the x axis: $S(\theta, 0)$. However, we assume that the actual gates we implement are given by Eq 3.5: $S'(\theta, \phi)$. Following the robustness condition, we can still achieve a very close $S(\theta, 0)$ gate using the composite pulse sequence below:

$$S'(\Theta, \phi_1)S'(\pi, \phi_2)S'(\Theta, \phi_1). \tag{3.12}$$

Here, the parameters Θ, ϕ_1, ϕ_2 can be determined by [54]:

$$\pi \sin \Theta = 2\Theta \cos(\theta/2), \tag{3.13}$$

$$\phi_1 = \arccos(-\pi \cos \Theta/(2\Theta \sin(\theta/2))), \tag{3.14}$$

$$\phi_2 - \phi_1 = -\arccos(-\pi/2\Theta). \tag{3.15}$$

The SCROFULOUS sequence can be extended to two-qubit systems, which means there is also a corresponding pulse sequence that can suppress systematic errors in two-qubit gates [55]. To understand this, we need to introduce first the concept of J-coupling error. We have introduced in Section 2.3 the exchange interaction $H = J\vec{S_1} \cdot \vec{S_2}$. For the Ising-type exchange interaction, the Hamiltonian simplifies to: $H = J\sigma_z \otimes \sigma_z/4$. Its time evolution operator can be written as $\exp(-iJt\sigma_z \otimes \sigma_z/4)$ (for simplicity, we set $\hbar$ = 1). Consequently, to get a specific $T(\Phi_1)$, we can just tune the evolution time such that $\Phi_1 = JT_1$. Therefore, for the systematic error in the $\Phi(1 + \epsilon)$, it is attributed to the errors in the J constant, which we refer as the J-coupling error.

The group theory and lie algebra allow us to associate a single qubit gate with an operator in a subgroup of SU(4) if the generators of this SU(4) satisfy the same commutation relations as the Pauli operators. This further leads to the fact that we can map the pulse length errors in single-qubit rotation operators to J-coupling errors in two-qubit operators. As a result, by replacing the single-qubit gates that constitute SCROFULOUS with their corresponding operators within this subgroup of SU(4), we can construct a SCROFULOUS sequence capable of implementing a two-qubit gate that is robust against systematic errors in the J-coupling. Following this mapping, we can have a two-qubit version of SCROFULOUS:

$$T(\zeta)S_2(-\theta, 0)T(\pi/2)S_2(\theta, 0)T(\zeta), \tag{3.16}$$

where we specifically choose the angles: $\zeta = -\frac{\pi}{4}\sec\theta, \sec\theta = -1.28$. Simplifying further, the pulse sequence can be rewritten as:

$$S_2(-\eta, 0)T(\pi/4)S_2(\eta, 0), \tag{3.17}$$

where $\tan\eta = \tan\theta\sec(\frac{\pi}{2}\sec\theta)$ and $S_2(\eta, 0) = I \otimes S(\eta, 0)$, indicating that the second qubit undergoes a single-qubit rotation. Fig 3.2 shows the quantum circuit of the two-qubit SCROFULOUS pulse sequence.

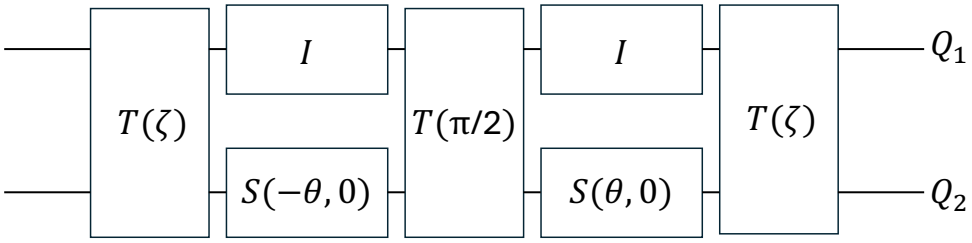

Figure 3.2: Schematic of the SCROFULOUS circuit. Q_1 and Q_2 represent the qubit 1 and qubit 2 respectively.

According to Eq 3.17, the composite pulse sequence Eq 3.16 is equivalent to a ZZ operator of $\Phi = \pi/4$ up to two single qubit rotations. This pulse sequence is designed based on the robustness condition which protects the ZZ gate in the middle against systematic errors in the exchange coupling. Suppose in practical situation, the elementary two-qubit operators within the pulse sequence: $T'(\zeta)S_2(-\theta, 0)T'(\pi/2)S_2(\theta, 0)T'(\zeta)$ contain errors. This composite pulse protocol achieves a better $ZZ_{\pi/4}$ gate compared with only one single pulse in the presence of the same fractional pulse error: $T'(\pi/4)$ (in later chapters, we refer it as the single-pulse protocol).

Fig 3.3 intuitively demonstrates that if we want to implement the $ZZ_{\pi/4}$, the SCROFULOUS has a higher average gate fidelity(see A.1) compared with a single-pulse ZZ gate over a certain range of systematic error in exchange coupling, which can also be referred to as J-tensor fractional error. Besides, this pulse sequence only contains three two-qubit operators in total which makes it much simpler than other types of composite pulse sequence.

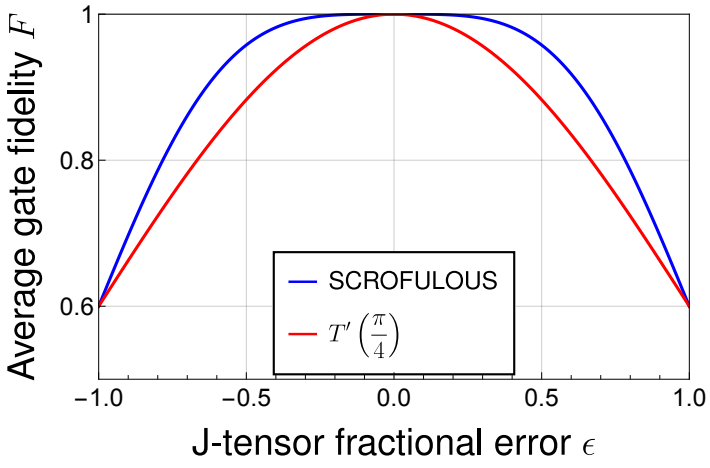

Figure 3.3: Comparison of $F(T'(\pi/4), ZZ_{\pi/4})$ and $F(\text{SCROFULOUS}, ZZ_{\pi/4})$ as a function of the J-tensor fractional error ϵ.

3.3.2. Broadband 1

Broadband 1 (BB1) is another composite pulses that is designed to be robust against the pulse length error. For $S(\theta, 0)$ the sequences provided below offers a highly accurate approximation, in which the $\phi = \cos^{-1}(-\theta/4\pi)$:

$$S'(\pi, \phi)S'(2\pi, 3\phi)S'(\pi, \phi)S'(\theta, 0), \tag{3.18}$$

$$S'(\theta, 0)S'(\pi, \phi)S'(2\pi, 3\phi)S'(\pi, \phi), \tag{3.19}$$

$$S'(\theta/2, 0)S'(\pi, \phi)S'(2\pi, 3\phi)S'(\pi, \phi)S'(\theta/2, 0). \tag{3.20}$$

As we can see that, the $S'(\pi, \phi)S'(2\pi, 3\phi)S'(\pi, \phi)$ serves as a correction pulse sequence to compensate for the errors.

BB1 can also be extended to a two-qubit version [57]. The sequence below effectively suppresses J-tensor fractional error of a ZZ operator, in which the ϕ is related to θ in the same manner as in the single-qubit case:

$$T'(\theta)S_2(\phi, 0)T'(\pi)S_2(-\phi, 0)S_2(3\phi, 0)T'(2\pi)S_2(-3\phi, 0)S_2(\phi, 0)T'(\pi)S_2(-\phi, 0). \tag{3.21}$$

There is a trade-off between the pulse sequence length and the robustness against errors. From the Fig 3.4 below we can see that, although BB1 has a much longer pulse sequence than SCROFULOUS, it demonstrates greater robustness against the errors.

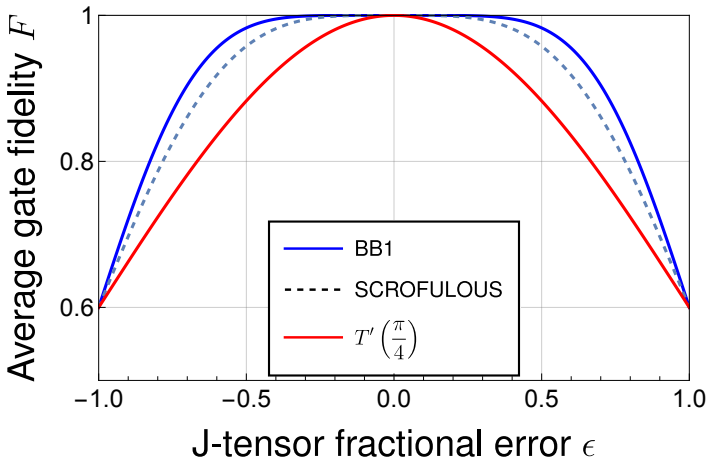

Figure 3.4: Comparison of $F(T'(\pi/4), ZZ_{\pi/4})$, $F(\text{SCROFULOUS}, ZZ_{\pi/4})$ and $F(\text{BB1}, ZZ_{\pi/4})$ as a function of the J-tensor fractional error ϵ. BB1's average gate fidelity is still close 1 even when the $\epsilon = 0.2$, meaning there is a 20% deviation of the J-tensor.

4

Protected Controlled-Z(CZ) gate

In this chapter, we investigate the physical implementation of a CZ gate that is protected against J-tensor fractional errors by employing the SCROFULOUS composite pulse sequence discussed in the previous chapter. Our study focuses on germanium-based hole spin qubits and uses the experimentally measured data provided in [58]. This chapter is divided into four sections: Section 4.1 establishes the theoretical framework for our two-qubit system; Section 4.2 focuses on leveraging the effective Hamiltonian to achieve the desired two-qubit operation; Section 4.3 introduces the method of g-tensor modulation which is important in realizing the middle process of SCROFULOUS; Section 4.4 discusses the practical implementation; Section 4.5 summarizes the simulation procedures and demonstrates the results.

4.1. Theoretical framework

A detailed derivation of this theoretical framework starting from the Fermi-Hubbard model is given in [59]. In this work, we focus on manipulating hole spins within the (1,1) charge stability region, where the first (second) value represents the number of holes in the left (right) dot. In the lab frame, the Hamiltonian can be expressed in the two-qubit basis: $\{|\uparrow\uparrow\rangle, |\uparrow\downarrow\rangle, |\downarrow\uparrow\rangle, |\downarrow\downarrow\rangle\}$ using the experimentally measured g-tensors and $\mathcal{J}$-tensor as follows:

$$H_{(1,1)}^{\text{lab}} = \frac{1}{2}\mu_B \vec{B} \cdot g_1 \vec{\sigma}_1 + \frac{1}{2}\mu_B \vec{B} \cdot g_2 \vec{\sigma}_2 + \frac{1}{4}\vec{\sigma}_1 \cdot \mathcal{J}\vec{\sigma}_2, \tag{4.1}$$

where, for simplicity, we set the $\hbar = 1$ in this and subsequent chapters. μ_B is the Bohr magneton, g_1 and g_2 correspond to the g-tensor of the first and second qubit, $\vec{\sigma}_1$ and $\vec{\sigma}_2$ are the Pauli vectors:

$$\vec{\sigma}_1 = (\sigma_{x,1}, \sigma_{y,1}, \sigma_{z,1}), \tag{4.2}$$

$$\vec{\sigma}_2 = (\sigma_{x,2}, \sigma_{y,2}, \sigma_{z,2}), \tag{4.3}$$

where $\sigma_{i,1} = \sigma_i \otimes I, \sigma_{i,2} = I \otimes \sigma_i, i \in \{x, y, z\}$ are the usual Pauli matrices and $\vec{B}$ is the magnetic field which we can express in the spherical coordinate: b is the strength, θ is the polar angle and ϕ is the azimuthal angle:

$$\vec{B} = b(\sin\theta\cos\phi, \sin\theta\sin\phi, \cos\theta). \tag{4.4}$$

Because the Hamiltonian needs to be hermitian and we have the freedom to choose a basis, g_1 and g_2 can be expressed by symmetric matrices for a given magnetic field. This enables Eq 4.1 to be rewritten as:

$$H^{\text{lab}}_{(1,1)} = \frac{1}{2}\mu_B g_1 \vec{B}\cdot\vec{\sigma}_1 + \frac{1}{2}\mu_B g_2 \vec{B}\cdot\vec{\sigma}_2 + \frac{1}{4}\vec{\sigma}_1\cdot\mathcal{J}\vec{\sigma}_2. \tag{4.5}$$

From Eq 4.5, we can always move into another frame by applying single qubit rotations R_1 and R_2 to the two Zeeman terms respectively to diagonalize them [59]:

$$\begin{aligned} H^{\mathcal{Q}}_{(1,1)} &= \frac{1}{2}\mu_B R_1(g_1\vec{B})\cdot\vec{\sigma}_1 + \frac{1}{2}\mu_B R_2(g_2\vec{B})\cdot\vec{\sigma}_2 + \frac{1}{4}\vec{\sigma}_1\cdot(R_1\mathcal{J}R_2^T)\vec{\sigma}_2 && (4.6)\\ &= \frac{1}{2}E_{z,1}\sigma_{z,1} + \frac{1}{2}E_{z,2}\sigma_{z,2} + \frac{1}{4}\vec{\sigma}_1\cdot\mathcal{J}^{\mathcal{Q}}\vec{\sigma}_2. && (4.7)\end{aligned}$$

In this new frame, the rotations R_1 and R_2 are applied such that $\mu_B R_1(g_1\vec{B}) = (0, 0, E_{z,1})$ and $\mu_B R_2(g_2\vec{B}) = (0, 0, E_{z,2})$. The R_1 (R_2) rotates the vector $g_1\vec{B}$ ($g_2\vec{B}$) to point in the $+z$ direction. These rotations must also be incorporated into the exchange coupling tensor $\mathcal{J}$, resulting in the transformed tensor $\mathcal{J}^{\mathcal{Q}} = R_1\mathcal{J}R_2^T$. The matrix representation of $\mathcal{J}^{\mathcal{Q}}$ is given by:

$$\begin{pmatrix} J^{\mathcal{Q}}_{xx} & J^{\mathcal{Q}}_{xy} & J^{\mathcal{Q}}_{xz} \\ J^{\mathcal{Q}}_{yx} & J^{\mathcal{Q}}_{yy} & J^{\mathcal{Q}}_{yz} \\ J^{\mathcal{Q}}_{zx} & J^{\mathcal{Q}}_{zy} & J^{\mathcal{Q}}_{zz} \end{pmatrix}. \tag{4.8}$$

This frame, referred to as the qubit frame, will be extensively used in the following sections.

4.2. Realization of the ZZ operator

With the theoretical framework clarified, we start explaining how we can implement the desired operators using the Hamiltonians mentioned above. The two-qubit version SCROFULOUS is presented in Eq 3.16, where the first pulse is a ZZ operator, $\exp(-i\zeta\sigma_z\sigma_z)$, with $\zeta = -\pi\sec\theta/4, \sec\theta = -1.28$. This operator can be realized starting from Eq 4.7. To simplify the notation, we use H_1 to replace $H^{\mathcal{Q}}_{(1,1)}$. We first move into the rotating frame (see A.3):

$$H_1^{rf}(t) = U^\dagger_{rf,1}(t)H_1U_{rf,1}(t) - iU^\dagger_{rf,1}(t)\left(\frac{d}{dt}U_{rf,1}(t)\right). \tag{4.9}$$

If we choose $U_{rf,1}(t)$ as:

$$U_{rf,1}(t) = \exp\left(-i\left(E_{z,1} + E_{z,2}\right)\left(\sigma_{z,1} + \sigma_{z,2}\right)t/4\right), \tag{4.10}$$

the $H_1^{rf}(t)$ will become:

$$H_1^{rf}(t) = \frac{1}{4}\left(E_{z,1} - E_{z,2}\right)\sigma_{z,1} + \frac{1}{4}\left(E_{z,2} - E_{z,1}\right)\sigma_{z,2} + U_{rf,1}^{\dagger}(t)\left(\frac{1}{4}\vec{\sigma}_1 \cdot \mathcal{J}^{\mathcal{Q}}\vec{\sigma}_2\right)U_{rf,1}(t). \tag{4.11}$$

The first two terms are merely phase terms which can be easily canceled out through compensation. This simplification leaves us with the effective Hamiltonian $\tilde{H}_1^{rf}(t)$ in the rotating frame:

$$\tilde{H}_1^{rf}(t) = U_{rf,1}^{\dagger}(t)\left(\frac{1}{4}\vec{\sigma}_1 \cdot \mathcal{J}^{\mathcal{Q}}\vec{\sigma}_2\right)U_{rf,1}(t). \tag{4.12}$$

By expressing $\tilde{H}_1^{rf}(t)$ in the matrix form and applying the Rotating Wave Approximation (RWA) in which all rapidly oscillating terms are neglected, we arrive at the following matrix representation:

$$\tilde{H}_1^{rf}(t) \approx \frac{1}{4}\begin{pmatrix} J_{zz}^{Q} & 0 & 0 & 0 \\ 0 & -J_{zz}^{Q} & J_{\perp} & 0 \\ 0 & J_{\perp}^{*} & -J_{zz}^{Q} & 0 \\ 0 & 0 & 0 & J_{zz}^{Q} \end{pmatrix}, \tag{4.13}$$

where the $J_{\perp} = J_{xx}^{Q} + J_{yy}^{Q} + i(J_{xy}^{Q} - J_{yx}^{Q})$.

As a result, we can see that if $|J_{zz}^{Q}|/|J_{\perp}| \gg 1$, the matrix above can be approximated by $J_{zz}^{Q}\sigma_z\sigma_z/4$. This implies that the time evolution operator of $\tilde{H}_1^{rf}(t)$ can be approximated by:

$$\exp(-iJ_{zz}^{Q}\sigma_z\sigma_z t/4). \tag{4.14}$$

To realize the desired two-qubit operator $\exp(-i\zeta\sigma_z\sigma_z)$, we simply need to control the evolution time t_1 such that: $t_1 = 1.28\pi/J_{zz}^{Q}$.

So far, we have successfully achieved the desired operator in the rotating frame:

$$\exp(-i\zeta\sigma_z\sigma_z) = U_p(t_1)U_1^{rf}(t_1) = U_p(t_1)\exp(-iH_1^{rf}t_1), \tag{4.15}$$

where the $U_p(t)$ is the phase compensation term we mentioned above:

$$U_p(t) = \exp(i(E_{z,1} - E_{z,2})(\sigma_{z,1} - \sigma_{z,2})t/4). \tag{4.16}$$

We can also have the desired operator directly from Eq 4.7 through the relation below [60]:

$$U_1(t) = \exp(-iH_1 t) = U_{rf,1}(t)U_1^{rf}(t). \tag{4.17}$$

Therefore, we can easily see that:

$$U_p(t_1)U_1^{rf}(t_1) = U_p(t_1)U_{rf,1}^{\dagger}(t_1)U_1(t_1) = U_p(t_1)U_{rf,1}^{\dagger}(t_1)\exp(-iH_1 t_1). \tag{4.18}$$

The $U_p(t_1)U_{rf,1}^{\dagger}(t_1)$ together can be viewed as one phase compensation operator. In summary, if we specifically design the evolution time of H_1 and calculate the exact phase for compensation, we can realize a desired ZZ operator using the double quantum dot system.

4.3. The middle three operators: one single process

As briefly introduced in Subsection 2.4.3, the correction terms in the anisotropic g-tensor enables it to be electrically modulated. In Subsection 4.3.1, we will discuss the practical method to electrically modulate the g-tensor during the simulation. In Subsection 4.3.2, we will explain the idea behind our motivation of implementing this g-tensor modulation and show how it is connected to the realization of the middle process of the SCROFULOUS pulse sequence.

4.3.1. Electric modulation of g-tensor

In Section 4.1 we pointed out that we have the freedom to choose the basis such that the g-tensor can be made a real symmetric matrix. This property enables the g-tensor to be decomposed into the form [58]:

$$R(\phi,\theta,\zeta)diag(g_{x'},g_{y'},g_{z'})R^{-1}(\phi,\theta,\zeta), \tag{4.19}$$

where ϕ,θ,ζ represent the zyz Euler angles, corresponding to a sequential rotations: a rotation around the original $+z$ axis by ϕ, followed by a rotation around the rotated $+y$ axis by θ, and finally, a rotation around the new $+z$ axis by ζ. These angles define the orientation of the principal axes of the g-tensor, denoted as x', y', z', with $g_{x'}, g_{y'}, g_{z'}$ representing the corresponding principal values. The explicit matrix representation of $R(\phi,\theta,\zeta)$ is given in A.4.

In experiments, the two hole spin qubits Q_1, Q_2 are approximately located underneath the corresponding plunger gates P_1, P_2. A sudden voltage change ΔV applied to the plunger gate or barrier gate near the quantum dot will induce variations in the six g-tensor components: $\phi,\theta,\zeta,g_{x'},g_{y'},g_{z'}$. Therefore, this enables us to electrically modulate the g-tensor by using the relation between the voltage change and the variations in these components. For small voltage variations, the changes in these quantities follow an approximate linear relation with ΔV:

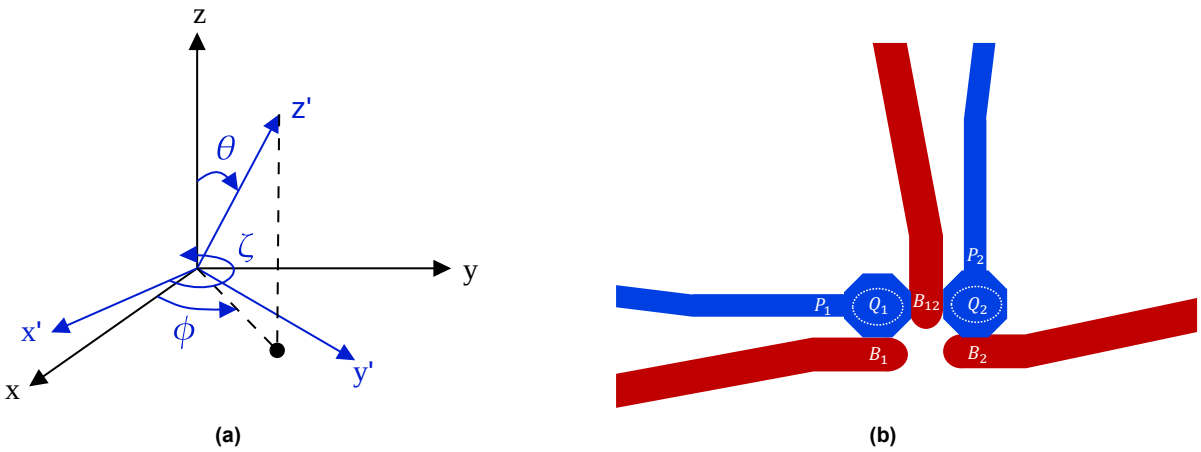

Figure 4.1: (a) Sketch of the six parameters in the g-tensor decomposition. (b) Schematic drawing of the related parts on the device. Q_1 and Q_2 represent the two quantum dots under the plunger gates P_1 and P_2. B_{12}, B_1, B_2 are the barrier gates. The figures are inspired by [58].

$$p' = p + \frac{dp}{dv}\delta V,\ p \in \{g_{x'}, g_{y'}, g_{z'}, \phi, \theta, \zeta\}. \tag{4.20}$$

Fig 4.1 presents a sketch of the six parameters representing the g-tensor decomposition, along with a schematic illustration of part of the device. For this thesis, we use the dataset measured in [58]. Explicit details can be found in B.2.

4.3.2. Realization of the middle process

Now consider the SCROFULOUS sequence:

$$U_{\text{seq}} = e^{-i\zeta\sigma_z\sigma_z} e^{i\frac{\theta}{2}I\sigma_x} e^{-i\frac{\pi}{2}\sigma_z\sigma_z} e^{-i\frac{\theta}{2}I\sigma_x} e^{-i\zeta\sigma_z\sigma_z}. \tag{4.21}$$

At first glance, the sequence might appear to involve five operators. However, we will show that by using the g-tensor modulation, the three middle operators can be effectively achieved as a whole only through a single process.

This method is based on an important condition: $e^{-iUAU^\dagger} = Ue^{-iA}U^\dagger$, where U is a unitary operator. The detailed proof of this relation is given in A.5. Therefore, if we can have a Hamiltonian that satisfies:

$$H_2 = e^{i\frac{\theta}{2}I\sigma_x} H_1 e^{-i\frac{\theta}{2}I\sigma_x}, \tag{4.22}$$

the time evolution of this Hamiltonian will be given by:

$$e^{-iH_2 t} = e^{i\frac{\theta}{2}I\sigma_x} e^{-iH_1 t} e^{-i\frac{\theta}{2}I\sigma_x}. \tag{4.23}$$

We have already shown in Section 4.2 that we can use H_1 to realize a ZZ operator by finding the phase compensation and deliberately tune the evolution time. In Sec-

tion 4.4, we will discuss in detail how to implement the phase compensation for this middle process. In this section, we first focus on how to obtain the desired H_2.

Plugging the expression of H_1 into the Eq 4.22, we find that the expression for H_2 is given by:

$$H_2 = e^{i\frac{\theta}{2}I\sigma_x}\left(\frac{1}{2}E_{z,1}\sigma_{z,1} + \frac{1}{2}E_{z,2}\sigma_{z,2} + \frac{1}{4}\vec{\sigma}_1 \cdot \mathcal{J}^{\mathcal{Q}}\vec{\sigma}_2\right)e^{-i\frac{\theta}{2}I\sigma_x} \tag{4.24}$$

$$= \frac{1}{2}E_{z,1}\sigma_{z,1} + \frac{1}{2}E_{z,2}\left(e^{i\frac{\theta}{2}I\sigma_x}\sigma_{z,2}e^{-i\frac{\theta}{2}I\sigma_x}\right) + \frac{1}{4}\vec{\sigma}_1 \cdot \mathcal{J}^{\mathcal{Q}}\left(e^{i\frac{\theta}{2}I\sigma_x}\sigma_{z,2}e^{-i\frac{\theta}{2}I\sigma_x}\right). \tag{4.25}$$

Analyzing this Hamiltonian, we observe that the two single qubit operators affect only the Pauli operators of qubit 2, while those of qubit 1 remain unchanged. Therefore, to simplify the calculation, we now focus on the Pauli operators of qubit 2. Using the matrix exponential, we can arrive at the following relation:

$$e^{i\frac{\theta}{2}\sigma_x}\sigma_z e^{-i\frac{\theta}{2}\sigma_x} = \sin\theta\sigma_y + \cos\theta\sigma_z. \tag{4.26}$$

We highlight here that this is equivalent to perform a linear transformation on the Pauli vector. The transformation matrix is exactly the rotation matrix $R_x(\theta)$:

$$R_x(\theta) = \begin{pmatrix} 1 & 0 & 0 \\ 0 & \cos\theta & -\sin\theta \\ 0 & \sin\theta & \cos\theta \end{pmatrix}, \tag{4.27}$$

$$\frac{1}{2}E_{z,2}\left(e^{i\frac{\theta}{2}I\sigma_x}\sigma_{z,2}e^{-i\frac{\theta}{2}I\sigma_x}\right) = \frac{1}{2}\mu_B R_2 g_2 \vec{B} \cdot (R_x(\theta)\vec{\sigma}_2) \tag{4.28}$$

$$= \frac{1}{2}(0, 0, E_{z,2}) \cdot (\sigma_x, \cos\theta\sigma_y - \sin\theta\sigma_z, \sin\theta\sigma_y + \cos\theta\sigma_z) \tag{4.29}$$

$$= \frac{1}{2}E_{z,2}(\sin\theta\sigma_y + \cos\theta\sigma_z). \tag{4.30}$$

Therefore, we can rewrite H_2 as follows:

$$H_2 = \frac{1}{2}E_{z,1}\sigma_{z,1} + \frac{1}{2}\mu_B R_2 g_2 \vec{B} \cdot (R_x(\theta)\vec{\sigma}_2) + \frac{1}{4}\vec{\sigma}_1 \cdot \mathcal{J}^{\mathcal{Q}}(R_x(\theta)\vec{\sigma}_2). \tag{4.31}$$

In the Subsection 4.3.1 we have mentioned that we can electrically modulate the g-tensor through applying voltage pulses. If we can numerically find a set of voltage difference $(\Delta V_{B_{12}}, \Delta V_{B_2}, \Delta V_{P_2})$ that transforms g_2 into g_2' which satisfies the following relation:

$$\frac{1}{2}\mu_B R_2 g_2 \vec{B} \cdot (R_x(\theta)\vec{\sigma}_2) = \frac{1}{2}\mu_B R_2 g_2' \vec{B} \cdot \vec{\sigma}_2, \tag{4.32}$$

we then achieve the ideal Hamiltonian whose time evolution operator can be tuned to obtain the desired ZZ operator.

The next steps are quite straightforward. We then control the evolution time of this Hamiltonian H_2. This evolution time should enable the middle operator in the $e^{i\frac{\theta}{2}I\sigma_x}e^{-iH_1t}e^{-i\frac{\theta}{2}I\sigma_x}$ to be equal to $e^{-i\frac{\pi}{2}\sigma_z\sigma_z}$ up to the phase factors. Let's denote this time as t_2, which can be calculated through the methods described in Section 4.2. It is found to be equal to $2\pi/J^Q_{zz}$, where J^Q_{zz} is still the element inside the Matrix 4.8. The final process of the SCROFULOUS sequence is the same ZZ operator as the first one. To implement this operator, we just tune the voltage of the three gates back to their original value at time $t = t_1 + t_2$. By doing this, we switch back the Hamiltonian to H_1. We simply let the system evolve again for t_1 to achieve the final ZZ operator. As a result, at the final time $t = 2t_1 + t_2$, we realize the SCROFULOUS pulse sequence.

From another perspective, if we consider the concept of basis transform, the three operators in the middle $e^{i\frac{\theta}{2}I\sigma_x}e^{-i\frac{\pi}{2}\sigma_z\sigma_z}e^{-i\frac{\theta}{2}I\sigma_x}$ can be viewed as one single operator in another basis. According to linear algebra, two orthonormal basis sets can be transformed into each other through a unitary operator. This means that if $\{|u_i\rangle\}$ and $\{|v_j\rangle\}$ are two orthonormal bases of a Hilbert space, this transformation can be represented by a unitary matrix U such that: $|v_j\rangle = \sum_i U_{ji}|u_i\rangle$. As a result, a quantum operator expressed in one of the orthonormal basis can be transformed into another using the same unitary matrix: for an operator A, its representation in the new basis is given by [45]:

$$A' = UAU^\dagger. \tag{4.33}$$

Suppose $e^{i\frac{\theta}{2}I\sigma_x}e^{-i\frac{\pi}{2}\sigma_z\sigma_z}e^{-i\frac{\theta}{2}I\sigma_x}$ corresponds to the the A in Eq 4.33, if we use $e^{-i\frac{\theta}{2}I\sigma_x}$ as the basis-transform unitary operator, the resulting operator in that new basis is actually a single ZZ operator:

$$e^{-i\frac{\theta}{2}I\sigma_x}\left(e^{i\frac{\theta}{2}I\sigma_x}e^{-i\frac{\pi}{2}\sigma_z\sigma_z}e^{-i\frac{\theta}{2}I\sigma_x}\right)e^{i\frac{\theta}{2}I\sigma_x} = e^{-i\frac{\pi}{2}\sigma_z\sigma_z}. \tag{4.34}$$

Therefore, it is reasonable to regard the three pulses as a single unified process, effectively performing a ZZ operator in the transformed basis.

One important point we need to notice is that the actual SCROFULOUS also contains two single qubit rotations, which according to Eq 3.17, is given by:

$$e^{-i\eta I\sigma_x}e^{-i\frac{\pi}{4}\sigma_z\sigma_z}e^{i\eta I\sigma_x}, \tag{4.35}$$

where $\tan\eta = \tan\theta\sec(\frac{\pi}{2}\sec\theta)$. We can also remove the two single qubit operators by finding the new basis in which the effect of this SCROFULOUS is truly a CZ gate.

4.4. Technical details

In Section 4.2 and 4.3, we have introduced the core idea and methods of implementing the SCROFULOUS composite pulse sequence. The Fig 4.2 below summarizes the

general workflow of the three processes in SCROFULOUS, illustrating how g-tensor modulation facilitates transitions between the processes. The figure also highlights the three requirements for implementing the ZZ gate using our hole double quantum dot system: a large $|J^Q_{zz}|/|J_\perp|$ ratio, the carefully tuned phase compensation and evolution time. In this section, we discuss in detail the practical implementation. This includes phase compensation, synchronization, and realization of large $|J^Q_{zz}|/|J_\perp|$.

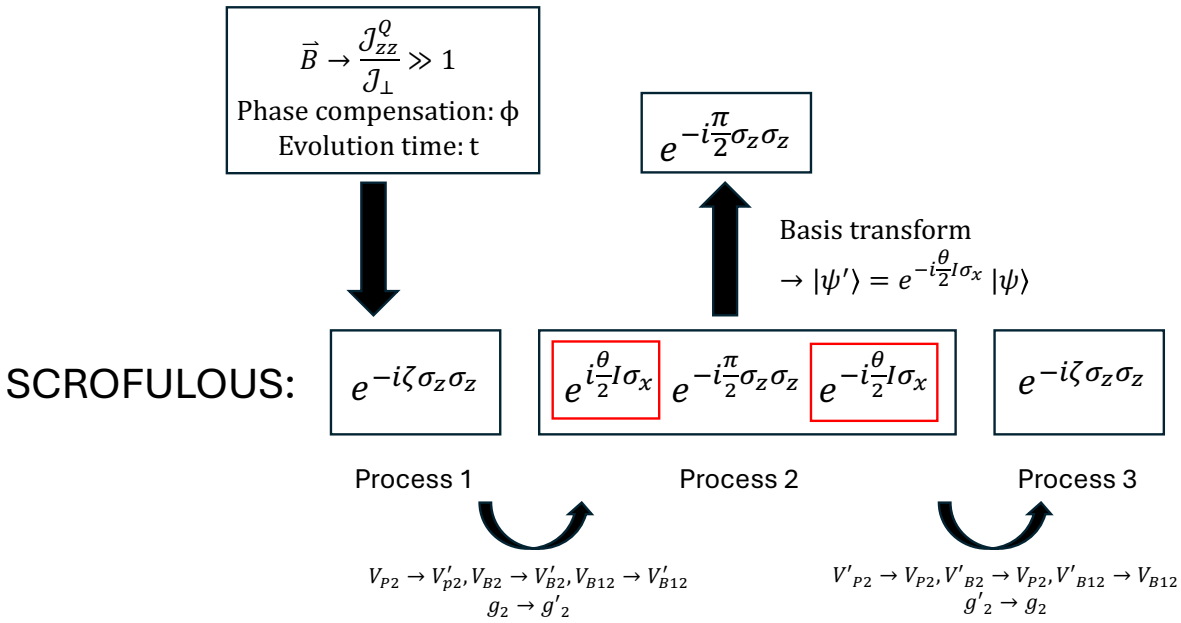

Figure 4.2: Overview of the SCROFULOUS three-process workflow.

4.4.1. Phase compensation

First, we notice from Eq 4.18 that the resulting expression contains single qubit phases $\exp(i\varphi_1\sigma_z I)$ and $\exp(i\varphi_2 I\sigma_z)$ that we need to compensate by applying the corresponding phase correction. The phase correction can be either performed before or afterwards. We note, that in an experiment, these phases can often be compensated digitally by Pauli Z updating.

For the first and the third process of SCROFULOUS, the resulting operator after the time evolution is approximately the following form:

$$\exp(i\varphi_1\sigma_z I)\exp(i\varphi_2 I\sigma_z)\exp(i\varphi_3\sigma_z\sigma_z). \tag{4.36}$$

Therefore, we can preset the phase for the first process: $\exp(-i\varphi_1\sigma_z I)\exp(-i\varphi_2 I\sigma_z)$ before the experiment starts. We notice that $\sigma_z I, I\sigma_z, \sigma_z\sigma_z$ commute with each other. Therefore, for the third process, we can add the compensation after the end of the total pulse sequence.

However, for the middle process, such a phase compensation cannot be realized digitally. In practical experiments, we can only tune the phase at the beginning or

at the end of the process. Due to this constraint, an additional operation is required, which is the focus of the next subsection: synchronization.

4.4.2. Synchronization

For the middle process, the resulting operator is given by:

$$\exp(i\theta I\sigma_x)\exp(-i\varphi_1\sigma_z I)\exp(-i\varphi_2 I\sigma_z)\exp(-i\varphi_3\sigma_z\sigma_z)\exp(-i\theta I\sigma_x). \tag{4.37}$$

Since σ_x and σ_z do not commute with each other, we can not manually cancel out the effect of $\exp(-i\varphi_2 I\sigma_z)$. To address this, we can tune some other parameters such that the resulting $\varphi_2 = 2\pi n,\ n \in \mathbb{Z}$, which makes $\exp(-i\varphi_2 I\sigma_z) = I$. In our case the parameter we can tune is the magnetic field strength and this operation is referred to as: synchronization. From Eq 4.7, we can easily calculate that the phase accumulation φ_2 in Eq 4.37 is given by:

$$\varphi_2 = \frac{1}{2}E_{z,2}t_2 = \frac{\pi E_{z,2}}{J^Q_{zz}} = \frac{\pi|\mu_B R_2(g_2\vec{B})|}{J^Q_{zz}} = 2\pi n. \tag{4.38}$$

Let its value be equal to $2\pi n$ and then we can calculate the suitable magnetic field strength through the equation:

$$|\mu_B R_2(g_2\vec{B})| = 2nJ^Q_{zz}. \tag{4.39}$$

Fig 4.3 visualizes the phase compensation and synchronization we apply during the experiment. The remaining operators in black constitute the SCROFULOUS pulse sequence.

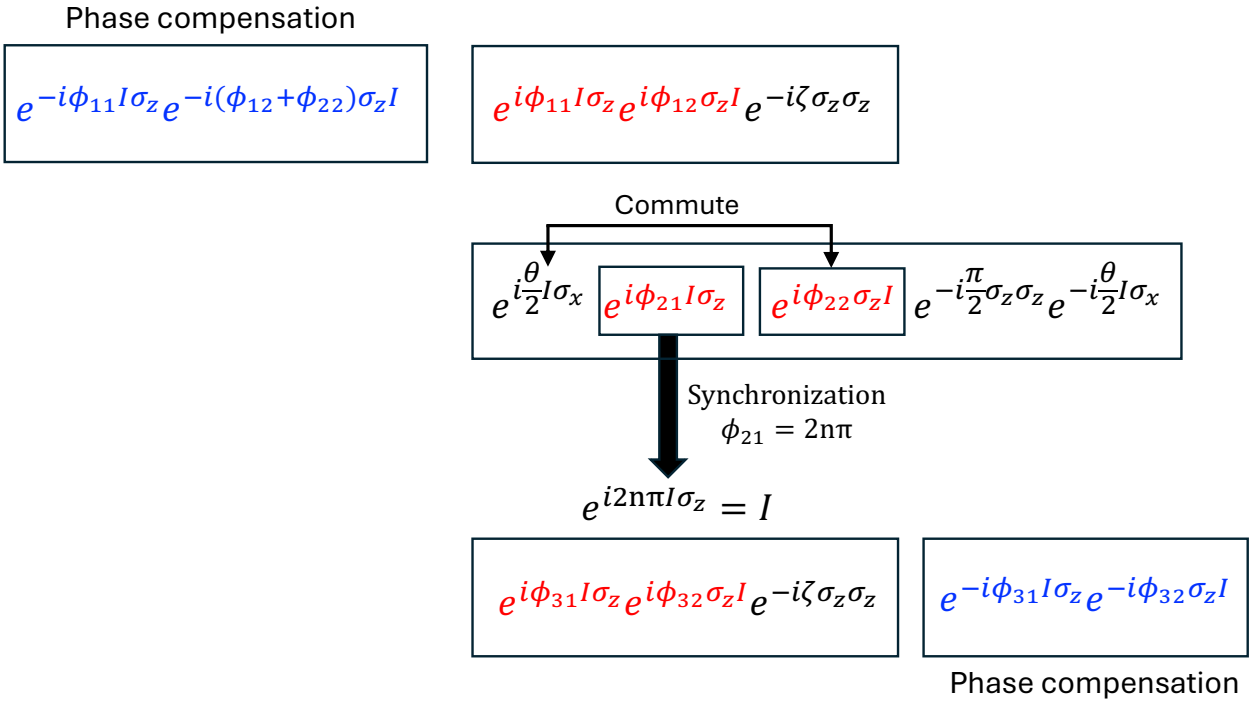

Figure 4.3: Sketch of phase compensation and synchronization.

4.4.3. Realization of large $|J^Q_{zz}|/|J_\perp|$

As mentioned before, the data we used primarily comes from the paper: [58] including the lab-frame g-tensors for the two germanium quantum dots, which is provided in B.1, and the measured corresponding voltage-induced change of the components in the decomposed g-tensor, also provided in B.2. However, this paper does not provide data of the lab frame $\mathcal{J}$-tensor. According to [59], the exchange interaction is actually a rotation matrix: $\mathcal{J} = \mathcal{J}_0 R_{\text{so}}(\Theta_{\text{so}})$, where R_{so} represents a rotation matrix around the direction of the spin-orbit field and Θ_{so} is related to the parameters such as the spin-orbit length and interdot distance. Therefore, we also use a rotation matrix to act as our $\mathcal{J}$-tensor. We assume the $\mathcal{J}$-tensor is given by:

$$\mathcal{J} = \mathcal{J}_0 \cdot R_z(\pi), \tag{4.40}$$

where $\mathcal{J}_0 = 0.2\pi\,\text{GHz}$ and this magnitude comes from [59]. The polar angle and the azimuthal angle of the magnetic field is: $1.600509\,\text{rad}$ and $0.244323\,\text{rad}$. The magnetic field strength is $0.510431\,\text{T}$. For this magnetic field, we find a quite large ratio for: $|J^Q_{zz}|/|J_\perp| \approx 1.78 \times 10^9$. The resulting exchange coupling term $\frac{1}{4}\vec{\sigma}_1 \cdot \mathcal{J}^Q\vec{\sigma}_2$ in the qubit-frame Hamiltonian after calculation is given by:

$$\begin{pmatrix} -0.157 & 0 & 0 & -0.139-0.282i \\ 0 & 0.157 & 0 & 0 \\ 0 & 0 & 0.157 & 0 \\ -0.139+0.282 & 0 & 0 & -0.157 \end{pmatrix}$$
$$+\begin{pmatrix} 0 & -3.2+4.2i & -2.4+4.7i & 0 \\ -3.2-4.2i & 0 & 0 & 2.4-4.7i \\ -2.4-4.7i & 0 & 0 & 3.2-4.2i \\ 0 & 2.4+4.7i & 3.2+4.2i & 0 \end{pmatrix} \times 10^{-6}$$
$$+\begin{pmatrix} 0 & 0 & 0 & 0 \\ 0 & 0 & -8.7+1.6i & 0 \\ 0 & -8.7-1.6i & 0 & 0 \\ 0 & 0 & 0 & 0 \end{pmatrix} \times 10^{-11}.$$

The voltage change set $(\Delta V_{B_{12}}, \Delta V_{B_2}, \Delta V_{P_2})$ we find is $(1081.81, -1253.04, 1283.82)$ with the unit in millivolts (mV).

We need to highlight here that a large ratio of $|J^Q_{zz}|/|J_\perp|$ is important for the realization of high-fidelity ZZ gate using the SCROFULOUS composite pulse sequence. We have already seen in Subsection 4.4.1 that the premise of expressing the time evolution operator as $\exp(i\varphi_1\sigma_z I)\exp(i\varphi_2 I\sigma_z)\exp(i\varphi_3\sigma_z\sigma_z)$ and implementing phase compensation is the commutation of $\sigma_z\sigma_z$ with $\sigma_z I$ and $I\sigma_z$. Therefore, if this exchange coupling term is not approximately an $\sigma_z\sigma_z$ operator in the rotating frame, which means the exchange coupling term contains off-diagonal operators,this will introduce undesired phase errors and quantum states transitions. The composite-pulse quantum gate is a non-adiabatic quantum gate, which means the error will easily accumulate during the process. Therefore, we need the $|J^Q_{zz}|/|J_\perp|$ to be large enough to suppress the error.

4.5. Results

Before we start discussing the simulation and results, there is one point that we need to pay attention to. In the original basis the J^Q_{zz} turns out to be negative as can be seen from the matrix form of $\frac{1}{4}\vec{\sigma}_1 \cdot \mathcal{J}^{\mathcal{Q}}\vec{\sigma}_2$. This makes the evolution time $t_1 = 1.28\pi/J^Q_{zz}$ and $t_2 = 2\pi/J^Q_{zz}$ also negative which is unrealistic. One way to transform $J^Q_{zz}\sigma_z\sigma_z$ into $-J^Q_{zz}\sigma_z\sigma_z$ is using the relation: $\sigma_x\sigma_z\sigma_x = -\sigma_z$. We can perform an additional basis transform in the qubit-frame on qubit 1 to transform Eq 4.7 into:

$$H^Q_{(1,1)} = \frac{1}{2}\mu_B R_x(\pi)R_1(g_1\vec{B})\cdot\vec{\sigma}_1 + \frac{1}{2}\mu_B R_2(g_2\vec{B})\cdot\vec{\sigma}_2 + \frac{1}{4}\vec{\sigma}_1\cdot(R_x(\pi)R_1\mathcal{J}R_2^T)\vec{\sigma}_2 \quad (4.41)$$
$$= -\frac{1}{2}E_{z,1}\sigma_{z,1} + \frac{1}{2}E_{z,2}\sigma_{z,2} + \frac{1}{4}\vec{\sigma}_1\cdot\mathcal{J}^{\mathcal{Q}}{}_{new}\vec{\sigma}_2. \quad (4.42)$$

For this $\mathcal{J}^{\mathcal{Q}}{}_{new}$, $J^Q_{zz,new} = -J^Q_{zz}$ which makes it a positive number and so do the $t_1 = 1.28\pi/J^Q_{zz} = 6.4\,\mathrm{ns}$ and $t_2 = 2\pi/J^Q_{zz} = 10\,\mathrm{ns}$.

We simulate the SCROFULOUS composite pulse sequence through the following procedures. We first define the time-dependent Hamiltonian:

$$H(t) = \begin{cases} H_1, & 0 \leq t < t_1 \\ H_2, & t_1 \leq t < t_1 + t_2 \\ H_1. & t_1 + t_2 \leq t \leq t_1 + 2t_2 \end{cases} . \tag{4.43}$$

At time $t = t_1$, we apply the voltage pulse $(\Delta V_{B_{12}}, \Delta V_{B_2}, \Delta V_{P_2})$ which tunes the g-tensor of qubit 2 and transforms the Hamiltonian from H_1 to H_2. At time $t = t_1 + t_2$, we turn off the voltage pulse to switch the Hamiltonian back to H_1. With the explicit form of this time-dependent Hamiltonian in hand, we can numerically solve the Schrödinger equation:

$$\frac{d}{dt}U(t) = -iH(t) \cdot U(t), \tag{4.44}$$

which gives us the unitary time evolution operator at time $t = t_1 + 2t_2$: $U(t_1 + 2t_2)$. Implementing the synchronization by finding the suitable magnetic field strength and adding the phase compensation, we can have the total unitary operator for the SCROFULOUS composite pulse sequence: Eq 4.21.

As mentioned in Subsection 4.3.2, the SCROFULOUS sequence contains two single qubit rotation. During the simulation, we manually remove these two operators through:

$$e^{I\eta I\sigma_x} \left(e^{-I\eta I\sigma_x} e^{-I\frac{\pi}{4}\sigma_z\sigma_z} e^{I\eta I\sigma_x} \right) e^{-I\eta I\sigma_x}. \tag{4.45}$$

Additionally, besides the pre-set phase compensation we need to apply, we can also add extra phase correction terms before and afterwards to further minimize the resulting gate infidelity. These extra phase correction terms can be calculated numerically.

Fig 4.4 demonstrates the average gate fidelity of the SCROFULOUS ZZ gate realized through hole spin qubits. We compare it with the same ZZ gate achieved through the single-pulse protocol, which is realized by simply let the Hamiltonian H_1 evolve for a time $\pi/J^Q_{zz} = 5\,\mathrm{ns}$ and implement corresponding phase compensation to the time evolution operator. Despite at the error-free point $\epsilon = 0$ the fidelity of the single-pulse ZZ gate is around 0.9998, which is a bit better than that of the SCROFULOUS ZZ gate: 0.9994, when the error starts to increase, the SCROFULOUS ZZ gate maintains a relatively higher fidelity while the fidelity of the single-pulse ZZ gate drops rapidly. For example, when the error reaches a value of $|\epsilon| = 0.3$, the fidelity of the SCROFULOUS ZZ gate is still higher than 0.990 while the fidelity of the single-pulse ZZ is only around 0.956. Therefore, we can conclude that the SCROFULOUS composite pulse scheme indeed suppresses the J-coupling error.

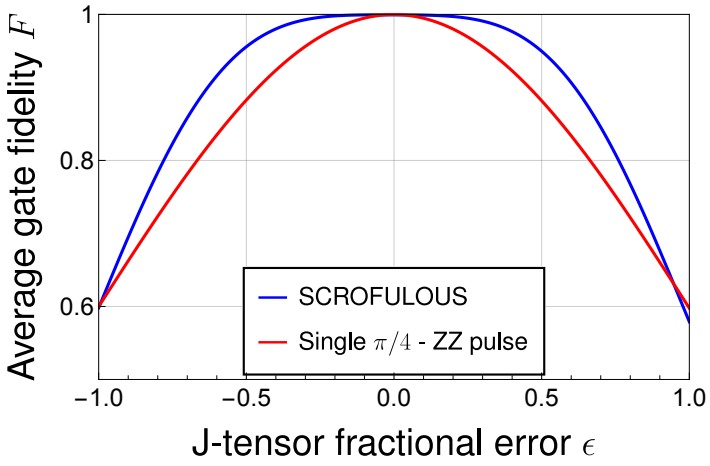

Figure 4.4: Comparison of the average gate fidelity of SCROFULOUS and the single-pulse ZZ gate between $ZZ_{\pi/4}$ as a function of the J-tensor fractional error ϵ.

Fig 4.5 compares the average gate fidelity of the SCROFULOUS ZZ gate realized through hole spin qubits with an ideal one. Fig 4.5(a) shows the general trend that for the negative J-tensor fractional error, the fidelity deviation of the physically-realized SCROFULOUS ZZ gate from the ideal gate is smaller compared to the case when the J-tensor fractional error is positive. This can be seen more clearly if we look at a smaller range: $\epsilon \in [-0.35, 0.35]$, which is shown in Fig 4.5(b). For example, when the $\epsilon = -0.3$, the fidelity of the physically-realized SCROFULOUS ZZ gate is 0.9927, with around 0.0015 lower than the ideal gate's fidelity. However, when the $\epsilon = 0.3$, the fidelity of the physically-realized SCROFULOUS ZZ gate drops to 0.9909, with around 0.003 lower than the ideal gate's fidelity. For the positive ϵ, this fidelity deviation between the physically-realized SCROFULOUS gate and an ideal SCROFULOUS gate actually increases with growth of ϵ, reaches a 0.02 deviation at $\epsilon = 1$.

In this section, we focused on the simulation of SCROFULOUS with only one type of error included: we only implemented the gate once and tested the J-tensor fractional error ϵ which remains constant during this gate operation. A more detailed investigation, testing and analysis on the robustness of SCROFULOUS follows in the next chapter.

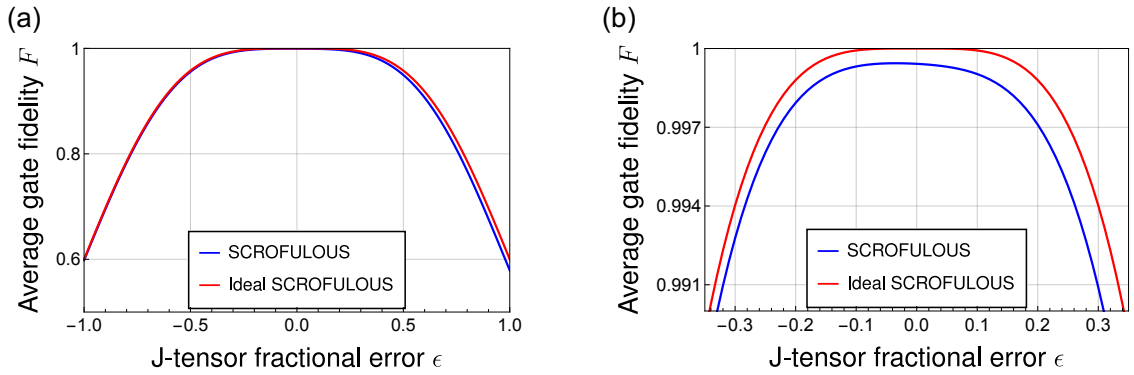

Figure 4.5: Comparison of the average gate fidelity of SCROFULOUS and an ideal SCROFULOUS between $ZZ_{\pi/4}$ as a function of the J-tensor fractional error ϵ: (a) $\epsilon \in [-1, 1]$. (b) $\epsilon \in [-0.35, 0.35]$.

5

Robustness Analysis

In this chapter, we investigate the performance of SCROFULOUS under various error scenarios, aiming to acquire a comprehensive understanding of its robustness. We will focus on the following types of error: quasi-static Gaussian J-tensor fractional error ϵ, voltage fluctuation induced by charge noise and errors introduced by ramp voltage change. We assume the quasi-static noise to be static during a single shot, but varies between different shots. Fig 5.1 gives a visualization of the experiments we will simulate in Section 5.1 and Section 5.2. For the simulation of implementing multiple gate operations, we employ the Monte Carlo method when calculating the average gate fidelity. For each specific gate number (N), we simulate the process for a large number of times and during each time a new random error or error set is picked depending on the type of error. Finally, we compute the mean value of all the resulting average gate fidelities. In the final part, we compare the SCROFULOUS ZZ gate with an adiabatic ZZ gate approach, highlighting their respective advantages and limitations.

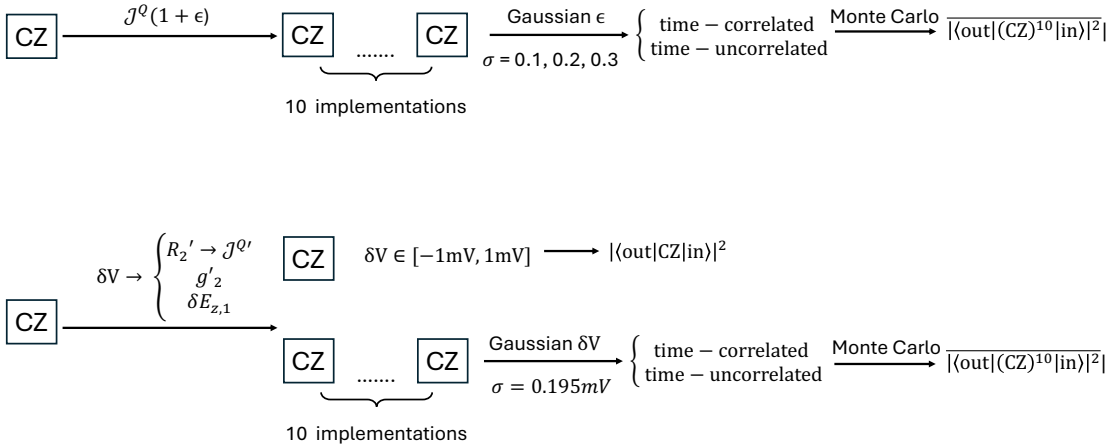

Figure 5.1: Visualization of the experiments we simulate in Section 5.1 and Section 5.2.

5.1. Modeling and analysis of Gaussian errors

In this section, we continue to focus on the J-tensor fractional error ϵ. However, instead of assuming a fixed value for this error, we now model it as a Gaussian error. In Subsection 5.1.1, we calculate and compare the expected process fidelity of the SCROFULOUS and single-pulse ZZ gate under this Gaussian error with different standard deviations. In Subsection 5.1.2, we study the scenario in which the SCROFULOUS and single-pulse ZZ gate are implemented consecutively multiple times in the presence of two types of quasi-static errors.

5.1.1. Comparison of expected process fidelity

We assume the Gaussian distributed J-tensor fractional error ϵ follows a distribution: $\epsilon \sim \mathcal{N}(0, \sigma^2)$, with a mean of zero and a standard deviation of σ. Therefore, the probability distribution of the Gaussian error is given by:

$$f(\epsilon, \sigma) = \frac{1}{\sigma\sqrt{2\pi}} \exp\left(-\frac{1}{2}\left(\frac{\epsilon}{\sigma}\right)^2\right). \tag{5.1}$$

We denote the erroneous ZZ gate implemented through SCROFULOUS as $U_{scro}(\epsilon)$ and the ZZ gate realized through the single-pulse protocol as $U_{ZZ}(\epsilon)$. Let U_i represent the ideal $\pi/4$ - ZZ operator and allow σ to vary within a small range, we can calculate and compare the corresponding expected process fidelity for these two quantum gate protocols, which is given by:

$$F_{\text{scro}} = \int_{-\infty}^{\infty} f(\epsilon) \frac{|tr(U_i^\dagger U_{scro}(\epsilon))|^2}{16}\, d\epsilon, \tag{5.2}$$

$$F_{\text{zz}} = \int_{-\infty}^{\infty} f(\epsilon) \frac{|tr(U_i^\dagger U_{ZZ}(\epsilon))|^2}{16}\, d\epsilon. \tag{5.3}$$

Fig 5.2 shows the resulting process fidelity when σ varies from 0.01 to 0.3. We note that errors with σ higher than 0.1 can already be considered as large errors. For these errors, we calculate and compare the corresponding process fidelities to show the capabilities of the composite pulse scheme. We focus on errors with smaller standard deviations, such as the region highlighted by the shaded area in Fig 5.2(a).

We have already shown in Section 4.5 that in ideal error-free case, the fidelity of the single-pulse ZZ gate will be slightly better than the SCROFULOUS ZZ gate. Fig 5.2(b) also demonstrates similar results. The data reveals that if the standard deviation of the error σ is smaller than 0.027, the process fidelity of the single-pulse ZZ gate is higher than that of the SCROFULOUS ZZ gate. For $\sigma = 0.01$, the process fidelity for single-pulse ZZ gate is 0.9996 while the process fidelity for SCROFULOUS ZZ gate is 0.99926. This phenomenon is caused by phase and non-adiabatic errors as already discussed in Subsection 4.4.3. The exchange interaction is only approximately a $\sigma_z\sigma_z$ operator in the rotating frame. The actual operator includes additional terms such as $\sigma_x\sigma_x$ and $\sigma_y\sigma_y$, which do not commute with $\sigma_z I$ and $I\sigma_z$. Such residual

non-adiabatic errors prevent us from obtaining a perfect ZZ gate through this composite pulse scheme.

However, when σ starts to increase, the process fidelity of the single-pulse ZZ protocol drops off rapidly while the SCROFULOUS shows a relatively slower decline and remains a fidelity above 0.99 even for $\sigma = 0.2$.

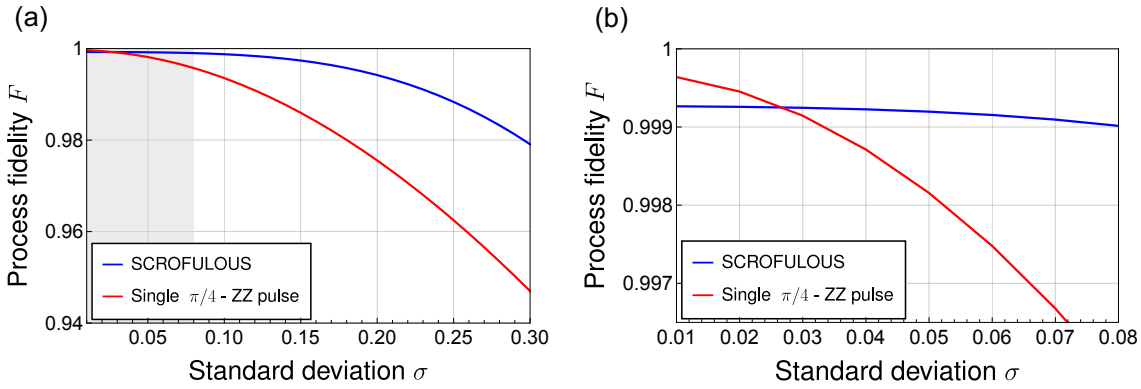

Figure 5.2: Comparison of the expected process fidelity as a function of the Gaussian error's standard deviation between the composite pulse protocol and the single-pulse protocol. (a) $\sigma \in [0.01, 0.3]$. (b) $\sigma \in [0.01, 0.08]$.

5.1.2. Multiple implementation of the quantum gates

In this subsection, we implement the quantum gates multiple times to analyze the accumulation of errors and their impact on the gate fidelity. We assume that the error still follows a Gaussian distribution: $\epsilon \sim \mathcal{N}(0, \sigma^2)$. We further assume the error to be quasi-static which remains static during a single shot, but varies between different shots. In the next paragraph, we provide a more detailed definition and distinguish between different types of quasi-static errors.

In the following simulation, we examine two types of quasi-static error, namely the time-correlated error and a time-uncorrelated error which emulates low-frequency noise on the time-scale of the gate time. We postpone the exact treatment to Chapter 6. It is important to remark that quasi-static error itself is time-correlated. Quasi-static error is defined as an error that remains static during a single shot. For the two types of error we examine, the time-correlated error means the error adopts the same value among subsequent gate operations, demonstrating a quite long correlation time. For the time-uncorrelated error, each subsequent gate experiences a different error. Therefore, we distinguish these two errors based on whether they show time-correlation among different gate operations. For the time-correlated error, the error value remains static during subsequent gate operation in a single circuit. For the time-uncorrelated error, we pick up a random value for each quantum gate we implement. The error is static for one single gate and varies between different gates.

For each type of error, we consider three different standard deviations for the error distribution: 0.1, 0.2, and 0.3 and we simulate quantum gates applied consecutively, ranging from 1 to 10 gates. As mentioned in Subsection 5.1.1, these are large errors showing the capabilities of the composite pulse scheme.

The Fig 5.3 and Fig 5.4 below show the results using 1000 Monte Carlo simulations. In general, we can see that for both time-correlated and time-uncorrelated error, the SCROFULOUS performs better than the single-pulse gate. Besides, the two figures reveal further insights regarding the error behavior and robustness of the SCROFULOUS scheme. In the following paragraphs, we will discuss these points in detail.

Firstly, we notice that when the number of gates applied increases, the fidelity of the single-pulse ZZ gate drops much quicker in the case of time-correlated error compared with the time-uncorrelated error. For SCROFULOUS, there is no such large difference between these two types of errors. The distinction arises due to how errors accumulate over multiple gate applications. For the time-correlated errors, the errors remain the same for all gates implemented, which leads to a coherent accumulation of the errors. This will result in a consistent drift, causing the final gate to deviate further from the ideal operation as more gates are applied. For example, for a single-qubit gate operation, if each gate operation has a fixed small angle deviation ϵ , after 10 operations, the total deviation will be amplified to 10ϵ. However, for the time-uncorrelated errors, the errors are randomly drawn from a Gaussian distribution at each gate application. The errors do not accumulate in a specific direction and may partially cancel out the effect of each other, similar to a random walk. This explains why the fidelity of the single-pulse ZZ gate decreases less rapidly for the time-uncorrelated errors.

In the previous paragraph, we pointed out the difference in the error accumulation pattern between the time-correlated and time-uncorrelated errors. Next, we will analyze the performance of SCROFULOUS in the presence of these two types of errors respectively. From Fig 5.3, we can see that the SCROFULOUS performs much better than the single-pulse ZZ gate, which is expected. The time-correlated errors remain fixed during each gate operation and can be regarded as reproducible systematic errors, which are exactly the type of errors that composite pulses are well designed to suppress [54].

From a frequency-domain perspective, time-correlated errors show lower frequencies compared to time-uncorrelated errors. According to our definition, For a constant time-correlated error, its frequency is approximately zero, while the error update frequency of the time-uncorrelated error is $1/T$, where T is the duration time of a single gate operation. As shown in Fig 5.4, we observe that although SCROFULOUS demonstrates suppression of time-uncorrelated errors, the fidelity difference between SCROFULOUS and the single-pulse ZZ gate is less significant compared to time-correlated errors. We also notice that, in Fig 5.4(c), as the number of gates increases, the fidelity of the single-pulse ZZ gate surpasses that of SCROFULOUS. This result is consistent with previous studies, which reported that some dynamical error suppression (DES) strategies perform poorly when dealing with errors that contain strong high-frequency components [61]. In Chapter 6, we will use the filter function to analyze the sensitivity of SCROFULOUS and the single-pulse ZZ gate to errors with different frequencies.

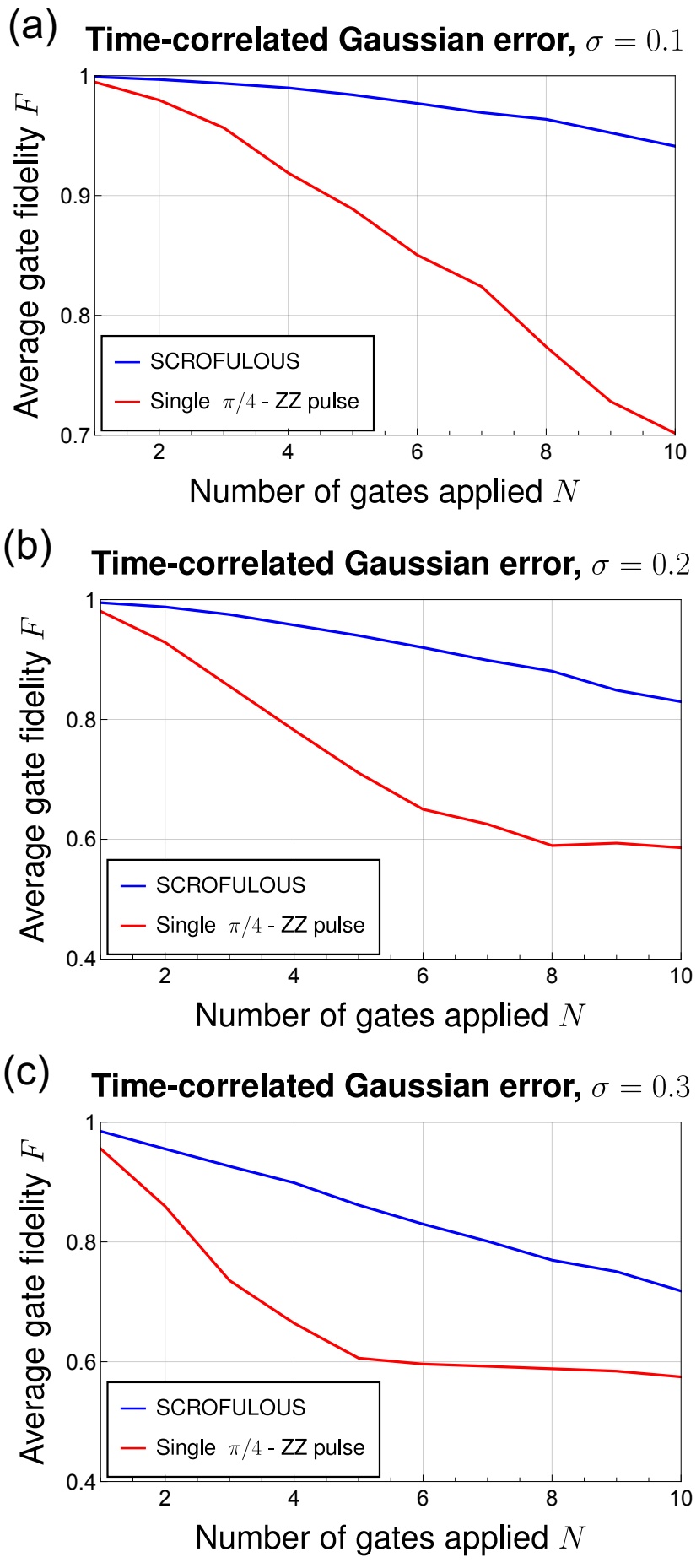

Figure 5.3: Comparison of the average gate fidelity calculated through Monte Carlo of SCROFULOUS and a single-pulse ZZ gate applied repeatedly multiple times for the time-correlated Gaussian J-tensor fractional error.

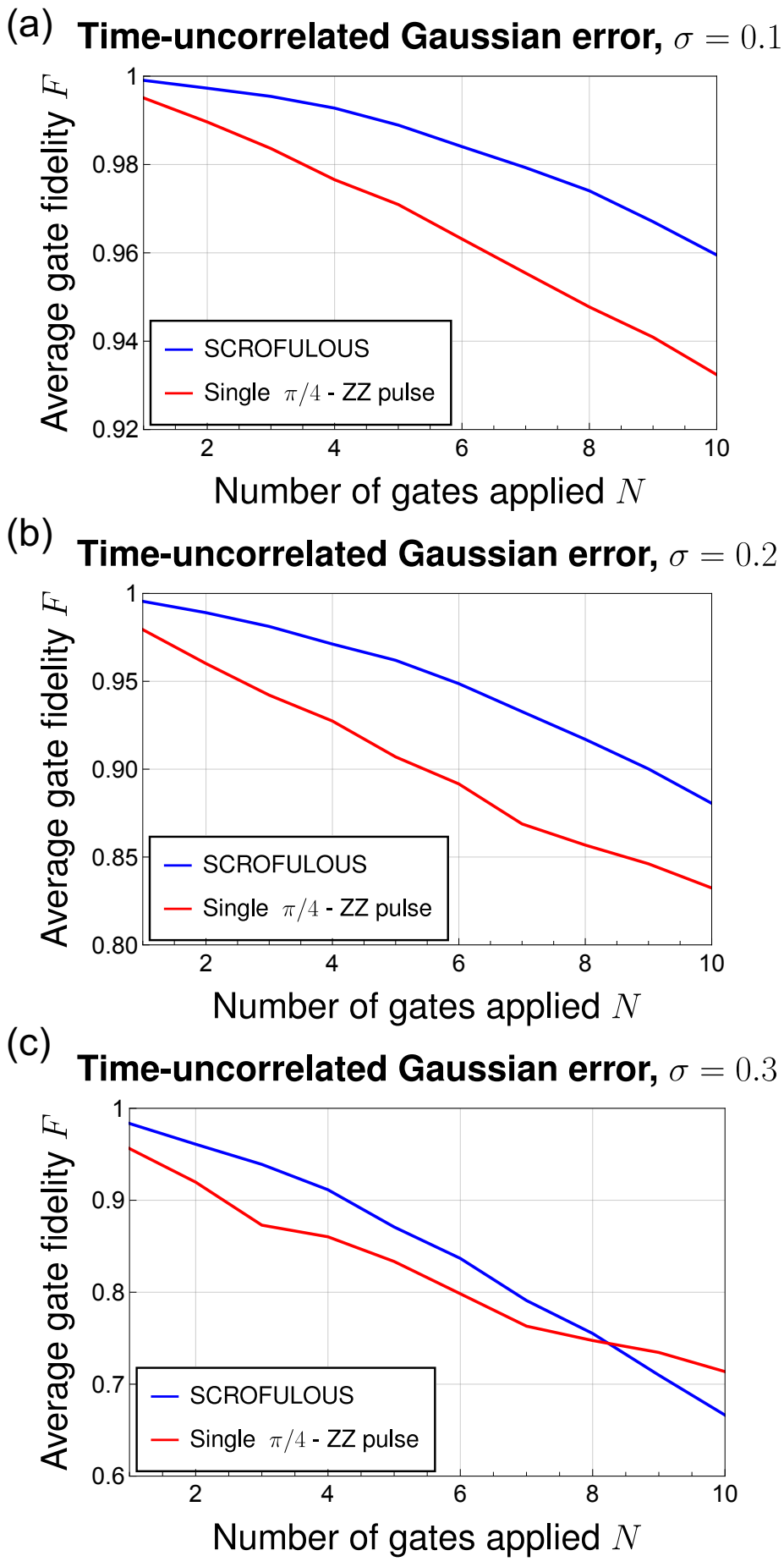

Figure 5.4: Comparison of the average gate fidelity calculated through Monte Carlo of SCROFULOUS and a single-pulse ZZ gate applied repeatedly multiple times for the time-uncorrelated Gaussian J-tensor fractional error.

5.2. Voltage fluctuation

Other than the J-tensor fractional error, another type of errors that may arise in experiments are voltage fluctuations. The physical origin of voltage fluctuations can be attributed to charge noise. Fig 5.5 illustrates the composition of a planar germanium heterostructure. The defects near the SiO_2-SiGe interface act as charge traps, which will lead to fluctuation of the number of carriers and ultimately cause voltage fluctuations [62]. From the Hamiltonian, we can see that voltage fluctuations will induce fluctuating Zeeman energies and fluctating Rotation matrices of the two qubits. We simulate this by considering a Gaussian-distributed voltage noise and analyze how this voltage noise affects the gate fidelity.

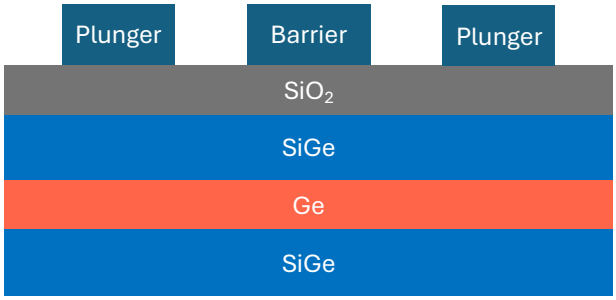

Figure 5.5: Schematics of a planar germanium heterostructure. Beneath the electrostatic gates, there is an oxide layer, with the dielectric material SiO_2 serving as an insulator. Below this layer lies the conventional SiGe-Ge-SiGe heterostructure.

For qubit 2, the perturbation to the Zeeman term caused by this voltage fluctuation is more intuitive. As discussed in Section 4.3, we can decompose the g-tensor into a rotated diagonal matrix characterized by three principal values and three rotation angles. The relation of how these parameters vary with voltage changes is also provided. Therefore, if we regard this voltage fluctuation δV as a small voltage pulse, the g-tensor can be expressed as: $g_2' = g_2(\delta V_{B12}, \delta V_{B2}, \delta V_{P2})$ where $\delta V_{B12}, \delta V_{B2}, \delta V_{P2}$ correspond to the voltage fluctuation on the barrier gates and plunger gate. We assume $\delta V_{B12} = \delta V_{B2} = \delta V_{P2} = \delta V$ for simplicity. Therefore, the Zeeman term becomes:

$$\frac{1}{2} R_2 g_2' \vec{B}. \tag{5.4}$$

For qubit 1, the effect of the voltage fluctuation on g-tensor is less straightforward because the paper [58] did not provide the corresponding data which characterize the voltage-induced change of the six parameters for qubit 1. However, in A.6, we give the detailed explanation of how the standard deviation of the Gaussian-distributed voltage fluctuation is connected to the dephasing time T_2^* which is provided in [58]. In the following paragraphs, we will estimate a suitable standard deviation and the first order correction of the Zeeman energy due to the voltage fluctuation for qubit 1.

We notice from the paper [58] that the dephasing time and magnetic field strength roughly exhibit an inverse proportional relation: $17.6\,\mu\mathrm{s}/9.2\,\mu\mathrm{s} \approx 35\,\mathrm{mT}/20\,\mathrm{mT}$. The magnetic field strength we use in our project is around $500\,\mathrm{mT}$ which, according to

the inverse proportionality, gives us an approximate dephasing time: $0.7\,\mu\mathrm{s}$. For the dimensionless α, we approximate it with the following expression:

$$\alpha = \left|\frac{\mu_B \vec{B}}{e}\right| \left|\overline{\frac{\partial g_{x'}}{\partial V}} + \overline{\frac{\partial g_{y'}}{\partial V}}\right| \tag{5.5}$$

$$= \left|\frac{\mu_B \vec{B}}{e}\right| \left|\frac{1}{3}\left(\frac{\partial g_{x'}}{\partial V_{B_{12}}} + \frac{\partial g_{x'}}{\partial V_{B_2}} + \frac{\partial g_{x'}}{\partial V_{P_2}}\right) + \frac{1}{3}\left(\frac{\partial g_{y'}}{\partial V_{B_{12}}} + \frac{\partial g_{y'}}{\partial V_{B_2}} + \frac{\partial g_{y'}}{\partial V_{P_2}}\right)\right|. \tag{5.6}$$

Due to the relatively large principal value $g_{z'}$, the magnetic field we find is very close to the xy-plane which gives us more freedom to tune the qubit quantization axis. Therefore, $\delta g_{x'}$ and $\delta g_{y'}$ should be the main contribution to the δg if we approximate the g-tensor in the first order: $g_1(\delta V) \approx g_1 + \delta g_1$. Following the relation $T_2^* = \sqrt{2}\hbar/\alpha e \sigma$ and plugging in the parameters with the correct unit, we found a standard deviation for the voltage fluctuation around: $\sigma = 0.195\,(\mathrm{mV})$. For the first-order correction of Zeeman energy $E_{z,1} = \alpha e \delta v$, we can express it as: $E_{z,1} = 0.01035 \cdot \delta V(\mathrm{GHz})$, in which we set $\hbar = 1$ and the δV is in the unit of mV.

Similar to our previous analysis of J-tensor fractional error, we first analyze the influence of a fixed voltage fluctuation value on the performance of a single gate operation. Based on the estimated standard deviation $\sigma = 0.195\,(\mathrm{mV})$, we assume the fluctuation lies within the range of $-1\,\mathrm{mV}$ to $1\,\mathrm{mV}$, which should encompass the vast majority of possible voltage fluctuation values. According to Fig 5.6, as the absolute value of voltage fluctuation increases, the average gate fidelity of SCROFULOUS decreases rapidly. However, the fidelity of the single-pulse ZZ gate shows no significant decline and remains at a high value close to 1.

The main factor that causes the rapid fidelity drop of SCROFULOUS is phase errors. In our Hamiltonian model, after we add the voltage fluctuation, the Zeeman energy for qubit 1 deviates from the ideal value with a correction term $E_{z,1}$. For qubit 2, however, not only does the Zeeman energy change, but the Zeeman term may also not remain diagonalized. In addition to $I\sigma_z$, other operators may also be present. SCROFULOUS has a longer gate time than the single-pulse ZZ gate which results in a larger phase error accumulation. Due to the voltage fluctuation, the g-tensor modulation we perform in SCROFULOUS is not accurate anymore, which introduces additional phase errors and non-adiabatic errors during the time evolution of the second process. Based on the results, we can have a preliminary conclusion that this composite pulse scheme is not robust against the voltage fluctuation error. It is sensitive to the charge noise. This result is also consistent with the conclusion in [54], which showed that SCROFULOUS is very sensitive to off-resonance errors.

We then perform the similar simulations as we do in Section 5.1. We implement the quantum gates consecutively multiple times with a quasi-static Gaussian voltage fluctuation, which can also be characterized as time-correlated or time-uncorrelated based on our previous definition. We then employ the same Monte Carlo method to calculate the average gate fidelity. Fig 5.7 illustrates the corresponding simulation

result, further confirming that SCROFULOUS is not robust against this type of quasi-static voltage fluctuation error.

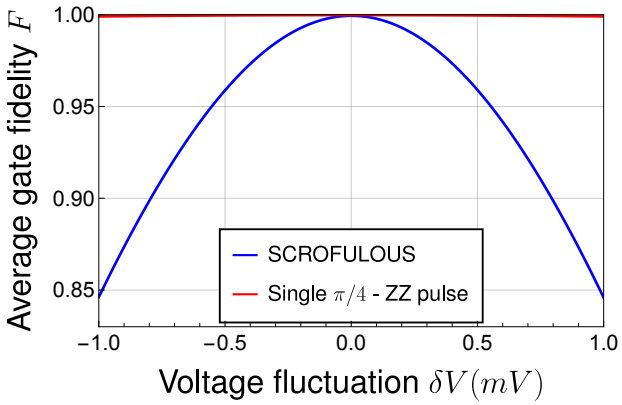

Figure 5.6: Comparison of the average gate fidelity of SCROFULOUS and the single-pulse ZZ gate between $ZZ_{\pi/4}$ as a function of the voltage fluctuation δV.

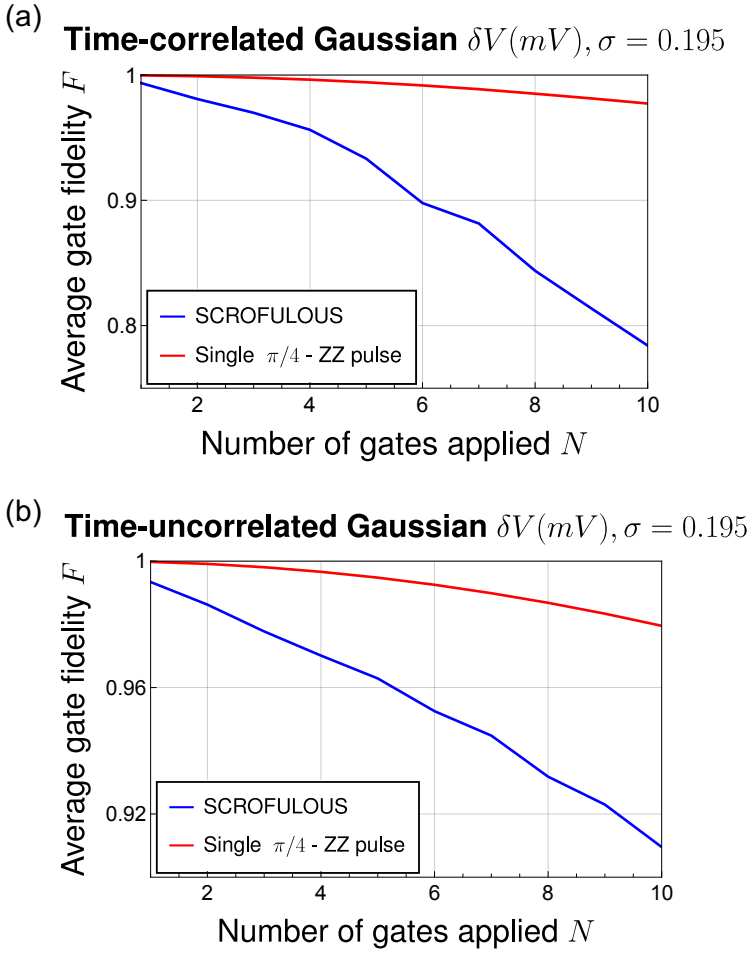

Figure 5.7: Comparison of the average gate fidelity calculated through Monte Carlo of SCROFULOUS and a single-pulse ZZ gate applied repeatedly multiple times for the (a) time-correlated (b) time-uncorrelated Gaussian voltage fluctuation δV.

5.3. Ramp voltage change

All our previous discussions have been based on the assumption that the voltage will instantaneously reach the pre-set value when voltage pulses are applied on the electrostatic gates. However, in practical experiments, achieving ultra-fast voltage changes imposes high demands on the precision and performance of the instruments. Meanwhile, if the voltage does not change instantaneously, the time evolution of the system during the voltage transition will accumulate errors. In this section, we simulate such a scenario: the voltages on the three gates simultaneously reach their pre-set values after a duration time T. During the process, the voltage changes linearly with time, which we also refer to as a ramp voltage pulse.

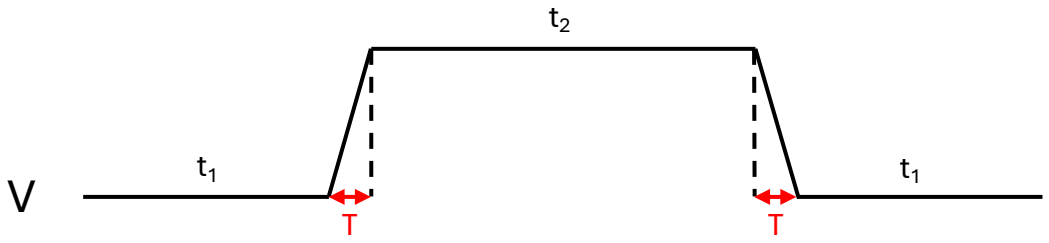

Figure 5.8: Schematic of the voltage pulse with a ramp transition time. t_1 and t_2 correspond to the time duration of the three time evolution processes in the SCROFULOUS sequence and T is the ramp time we assume.

Fig 5.8 shows a schematic illustration of how the voltage changes with a ramp time. Based on the plot, we can express the voltage change as a time-dependent equation. Taking the voltage change on the plunger gate ΔV_{P2} as an example, its expression is given by:

$$\Delta V_{P2} = \begin{cases} 0, & 0 \leq t < t_1 \\ 1283.8187(t - t_1)/T, & t_1 \leq t < t_1 + T \\ 1283.8187, & t_1 + T \leq t < t_1 + t_2 + T \\ 1283.8187(t_1 + t_2 + 2T - t)/T, & t_1 + t_2 + T \leq t < t_1 + t_2 + 2T \\ 0. & t_1 + t_2 + 2T \leq t < 2t_1 + t_2 + 2T \end{cases}$$

The voltage changes on the two barrier gates: ΔV_{B2} and ΔV_{B12} follow the same time-dependent relation.

Remember that the g-tensor variation will also lead to change in the exchange coupling tensor $\mathcal{J}^{\mathcal{Q}} = R_1 \mathcal{J} R_2^T$ through the rotation matrix. Suppose R_2 denotes the original rotation matrix for qubit 2 and R_2' corresponds to the one after the voltage change. For simplicity, we assume the rotation matrix during this ramp transition $\tilde{R}_2(t)$ also follows a linear interpolation:

$$\tilde{R}_2(t) = \begin{cases} R_2, & 0 \le t < t_1 \\ R_2'(t-t_1)/T + R_2(t_1+T-t)/T, & t_1 \le t < t_1+T \\ R_2', & t_1+T \le t < t_1+t_2+T \\ R_2'(t_1+t_2+2T-t)/T + R_2(t-t_1-t_2-T)/T, & t_1+t_2+T \le t < t_1+t_2+2T \\ R_2. & t_1+t_2+2T \le t < 2t_1+t_2+2T \end{cases}$$

As demonstrated in Fig 5.9, the fidelity of the SCROFULOUS ZZ gate is very sensitive to the ramp time. Fig 5.9(a) shows the region where the ramp time ranges from 0 to $1\,\mathrm{ns}$. We can observe a dramatic fidelity fluctuation which is because of the phase error introduced by the high-frequency Zeeman terms in the Hamiltonian. Fig.5.9(b) extends the range of the ramp time, where we can observe an interference pattern. From this result, we can acquire the conclusion that: if the instruments cannot achieve the pre-set voltage value within an extremely short time, the introduced phase error will significantly influence the gate performance. Therefore, it is necessary to consider ways to mitigate this effect.

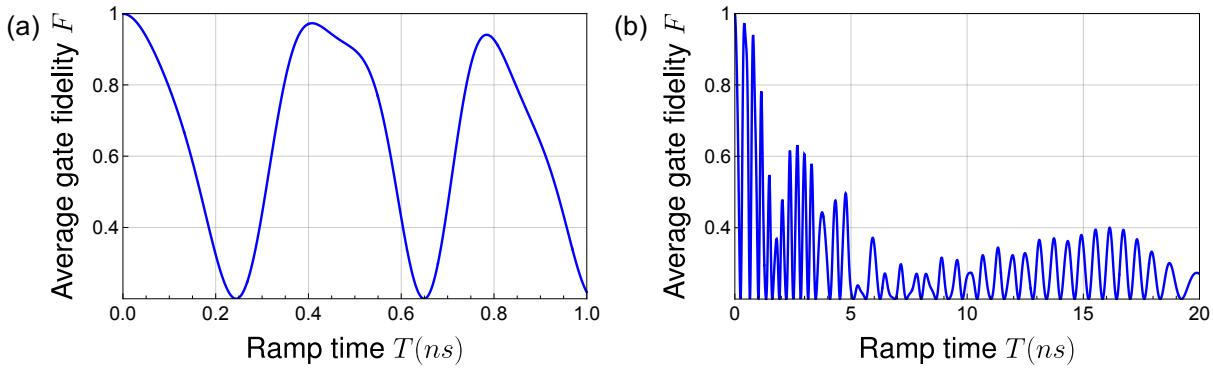

Figure 5.9: The average gate fidelity of SCROFULOUS as a function of the ramp transition time.

5.4. SCROFULOUS vs adiabatic quantum gate

Currently, one of the commonly adopted approaches to achieving high-fidelity two-qubit gates is through the adiabatic quantum gate protocol. In this section, we first propose a hypothetical method to implement an adiabatic ZZ gate using our double-quantum-dot hole spin qubit system and compare this protocol with our SCROFULOUS ZZ gate to analyze their robustness.

According to the adiabatic theorem, the system Hamiltonian needs to vary slowly enough such that the system can maintain in the instantaneous ground state without being excited to higher energy states [63]. Therefore, the exchange interaction should be gradually turned on and off to avoid sudden changes in the Hamiltonian. Based on this requirement, we design the adiabatic Hamiltonian to be:

$$H_{ad} = \frac{1}{2}E_{z,1}\sigma_{z,1} + \frac{1}{2}E_{z,2}\sigma_{z,2} + \frac{1}{18.24}\left(1 - \cos\left(\frac{2\pi t}{T_{tot}}\right)\right)\vec{\sigma}_1 \cdot \mathcal{J}^{\mathcal{Q}}\vec{\sigma}_2, \tag{5.7}$$

where the T_{tot} represents the total duration time of SCROFULOUS which equals to $4.56\pi/J^{Q}_{zz}$. We assume the gate operation time is equal for both gate protocols to make the comparison results more fair. The$(1-\cos(2\pi t/T_{tot}))/4.56$ is multiplied in the exchange coupling term to gradually switch on and off the exchange coupling and achieve the desired amount of phase at the time point $t = T_{\text{tot}}$.

With the adiabatic Hamiltonian introduced, we compare this adiabatic-protocol ZZ gate with the SCROFULOUS ZZ gate, focusing on their robustness to the J-tensor fractional error and the voltage fluctuations. Fig 5.10 shows the performance of the two gate protocols in the presence of these two errors. Similar to the results we got from previous sections, the SCROFULOUS ZZ gate is more robust against the J-tensor fractional error while performs less well than the adiabatic ZZ gate regarding on the voltage fluctuations.

In Fig 5.11, we make a more direct comparison by calculating the fidelity difference between them: $\Delta F = F_{\text{SCROFULOUS}} - F_{\text{adiabatic}}$. From this plot, we can clearly see that although the SCROFULOUS ZZ gate performs worse than the adiabatic gate when there is no J-tensor fractional error and only voltage fluctuation, its fidelity outperforms that of the adiabatic gate in the regions where both errors exist simultaneously. When the voltage fluctuations are not too large, and the J-tensor fluctuation error is also present in the system, SCROFULOUS demonstrates better performance. This highlights the advantage of SCROFULOUS gate protocol over adiabatic protocols because in actual operations, these two errors may occur simultaneously.

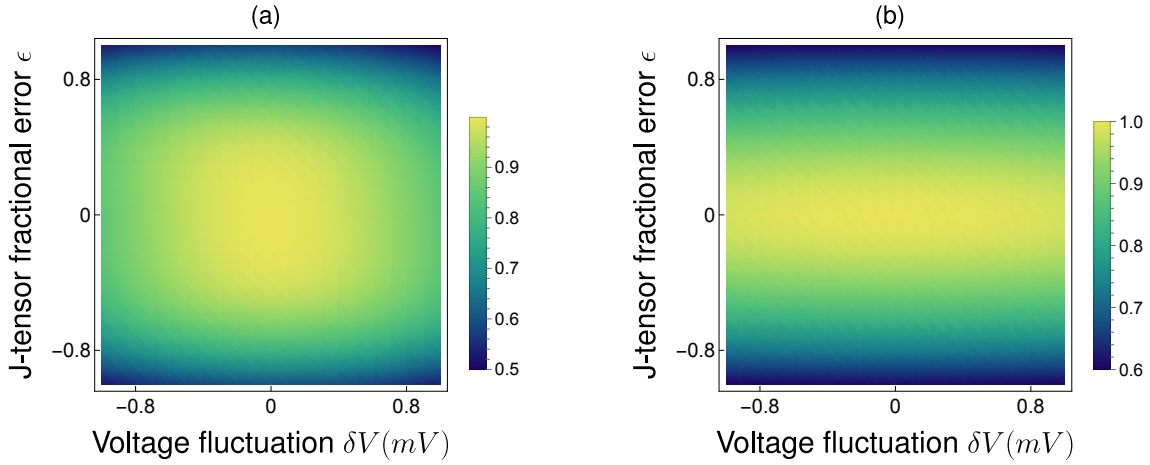

Figure 5.10: Fidelity density plot of the ZZ gate in the presence of both the J-tensor fractional error ϵ and voltage fluctuation δV: (a) SCROFULOUS. (b) Adiabatic ZZ gate.

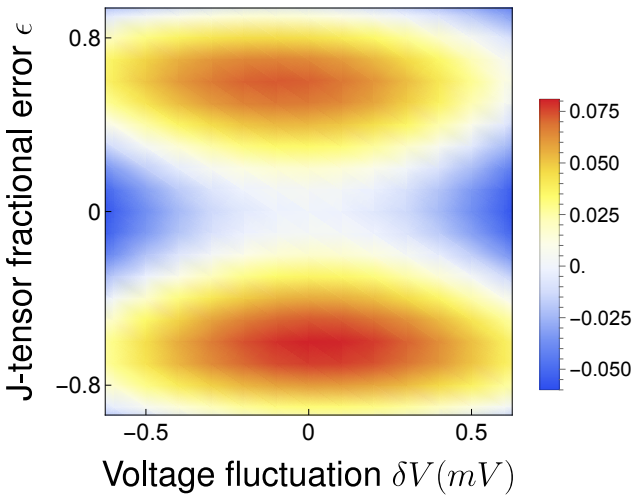

Figure 5.11: The difference in fidelity between the SCROFULOUS ZZ gate and the adiabatic ZZ gate at the same point $(\delta V, \epsilon)$.

6

Filter Function Formalism

The filter function formalism is a powerful mathematical framework developed in the field of quantum control theory. Quantum control methods such as dynamical decoupling protocols and composite pulses are specially designed to decouple the system from interference of environmental noise or systematic errors. The filter function formalism can be used to characterize the performance of these protocols by calculating the overlap between the noise's power spectral density (PSD) and the spectral susceptibility of these protocols to noise at different frequencies which is the so-called filter function [64].

Following the derivation provided in [64], we briefly demonstrate how the filter function can describe the influence of noise and its connection to the average gate fidelity, using the example of purely dephasing noise in single-qubit control. In this case, the noise Hamiltonian can be modeled as:

$$H_n(t) = \beta_z(t)\sigma_z. \tag{6.1}$$

The fidelity here is defined as the ensemble average of process fidelity in which all realizations of the noise Hamiltonian Eq 6.1 are considered. According to [64], the fidelity can be expressed as a series expansion in terms of a so-called error vector. Assuming we are in the weak noise regime which allows us to ignore higher order expansion terms, the fidelity, after controlling the qubit to evolve for a time interval $[0, \tau]$, can be written as:

$$F = 1 - \sum_{i=x,y,z} \int_0^\tau dt_2 \int_0^\tau dt_1 \langle \beta_z(t_1)\beta_z(t_2)\rangle R_{zi}(t_1)R_{zi}(t_2), \tag{6.2}$$

where $C(t_1, t_2) = \langle \beta_z(t_1)\beta_z(t_2)\rangle$ denotes the noise correlation function at two time points: t_1, t_2 and $R_{zi}(t_1), R_{zi}(t_2), i \in \{x, y, z\}$ are elements of the so-called control matrix which, we will see later, are directly related to the filter function.

If we further require the noise to be at least weakly stationary, which enables the $C(t_1, t_2)$ to be written as $C(|t_1 - t_2|)$, the cross-correlation function can be further

expressed in the frequency domain as:

$$\langle \beta_z(t_1)\beta_z(t_2)\rangle = \frac{1}{2\pi}\int_{-\infty}^{\infty} d\omega S_{zz}(\omega)e^{i\omega(t_2-t_1)}. \tag{6.3}$$

Here $S_{zz}(\omega)$ represents the power spectral density (PSD) of the noise. If we relate $e^{i\omega t_2}$ to $R_{zi}(t_2)$ and $e^{-i\omega t_1}$ to $R_{zi}(t_1)$, and define the following Fourier transform:

$$R_{ij}(\omega) \equiv -i\omega \int_0^{\tau} dt R_{ij}(t)e^{i\omega t}, \tag{6.4}$$

we can express the fidelity as:

$$F = 1 - \frac{1}{2\pi}\sum_{i=x,y,z}\int_{-\infty}^{\infty}\frac{d\omega}{\omega^2}S_{zz}(\omega)R_{zi}(\omega)R^*_{zi}(\omega) \tag{6.5}$$

$$= 1 - \frac{1}{2\pi}\sum_{i=x,y,z}\int_{-\infty}^{\infty}\frac{d\omega}{\omega^2}S_{zz}(\omega)|R_{zi}(\omega)|^2. \tag{6.6}$$

As a result, we then automatically have the first-order filter function defined as:

$$F_z^{(1)}(\omega) = \sum_{i=x,y,z}|R_{zi}(\omega)|^2. \tag{6.7}$$

In the weak noise regime where the higher order expansion terms in error vectors are ignored, the fidelity Eq 6.2 can also be approximated as:

$$F = \frac{1}{2}(1+\exp[-\chi(\tau)]), \tag{6.8}$$

where in this form, $\chi(\tau)$ is the function characterize the fidelity decay:

$$\chi(\tau) = \int_0^{\infty}\frac{d\omega}{\omega^2}S_{zz}(\omega)F_z^{(1)}(\omega). \tag{6.9}$$

This $\chi(\tau)$ can also be derived through the qubit density matrix formalism and be used to describe the decoherence [65]. From Eq 6.8 we find that if we want to prevent the decay of the gate fidelity, we need to let the $\chi(\tau)$ as close to 0 as possible. Therefore, $F_z^{(1)}(\omega)$ should approach 0 in regions where $S_{zz}(\omega)$ is large, effectively filtering out the noise. This characteristic is the reason why it is referred to as a filter function.

In the rest of this chapter, we first give a detailed derivation and calculation of the filter function for two-qubit systems which is inspired by [64, 66]. Based on that, we calculate and plot the filter function for the SCROFULOUS composite pulse protocol.

6.1. The filter function for two-qubit systems

Suppose our system is subject to ZZ-type noise. The effective Hamiltonian now is given by:

$$H_e = H^Q_{(1,1)} + \delta\beta(\sigma_z \otimes \sigma_z), \tag{6.10}$$

where $\delta\beta$ represents the strength of the fluctuating term. Here, $H^Q_{(1,1)}$ is the qubit-frame Hamiltonian given in Eq 4.7. It is now regarded as the control Hamiltonian and its time evolution operator is denoted as: $U_c(t)$. Moving into the interaction picture with respect to the control term, the effective Hamiltonian becomes:

$$H_e^{int} = \delta\beta U_c^\dagger(t)\,(\sigma_z \otimes \sigma_z)\,U_c(t). \tag{6.11}$$

In practical situations, the intensity of the noise is usually dependent on the frequency. For example, a common type of noise in solid-state devices such as semiconductor quantum dots or superconducting qubits is $1/f$ noise [67]. Its PSD is inversely proportional to the frequency: $S(\omega) \propto 1/f$. The noise intensity increases as the frequency decreases and reaches a high value at very low frequencies. Therefore, we need to include the frequency information in the noise term. This can be achieved by substituting the $\delta\beta$ with $\tilde{\delta\beta} = \delta\beta e^{i2\pi ft}$ which is now a complex term with frequency f included. The Hamiltonian now reads:

$$\tilde{H}_e^{int} = \tilde{\delta\beta} U_c^\dagger(t)(\sigma_z \otimes \sigma_z)U_c(t). \tag{6.12}$$

From this Hamiltonian, we can now calculate the first-order filter function according to the following integral:

$$F_{zz}(f) = \frac{1}{\delta\beta T}\int_0^T \tilde{H}_e^{int}(f,\tau)\,d\tau. \tag{6.13}$$

The Hilbert space of a two-qubit system is a four-dimensional complex vector space. It is spanned by the tensor product of Pauli matrices and the identity matrix. The basis can be represented as: $P_i \otimes P_j \,|\, P_i, P_j \in \{I, \sigma_x, \sigma_y, \sigma_z\}$ which forms an orthogonal basis for all 4×4 matrices under the Hilbert-Schmidt inner product. This property allows us to decompose $F_{zz}(f)$ as:

$$F_{zz}(f) = (F_{zzIx}(f), ..., F_{zzzz}(f)) \cdot (I \otimes \sigma_x, ..., \sigma_z \otimes \sigma_z), \tag{6.14}$$

where we ignore the trivial $I \otimes I$ component. Using the orthogonality and considering the normalization factor, we can calculate the corresponding component:

$$F_{zz\otimes ij}(f) = \frac{1}{4}Tr[F_{zz} \cdot (\sigma_i \otimes \sigma_j)]. \tag{6.15}$$

The magnitude of the $F_{zz}(f)$ is consequentially given by:

$$|F_{zz}(f)| = F^2_{zzIx}(f) + ... + F^2_{zzzz}(f). \tag{6.16}$$

6.2. The filter function of SCROFULOUS

The previous section demonstrated how to compute the filter function for a two-qubit system under a single noisy process. For quantum control protocols such as dynamical decoupling and composite pulse scheme, they normally include sequences of control operations designed to mitigate noise and enhance coherence. The Fig 6.1 shows the diagram for a piecewise-defined control sequence. For example, in the case of the CPMG dynamical decoupling protocol, the control operations consist of π-pulses applied at times $t = t_l, l \in [1, n-1]$ and $\pi/2$-pulses applied at time $t = t_0$ and $t = t_n$.

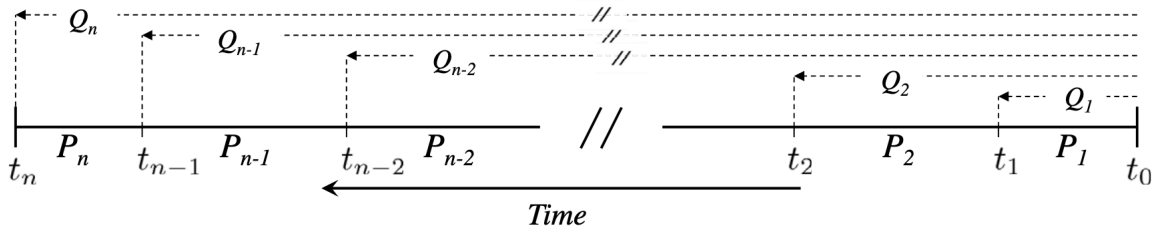

Figure 6.1: Illustration of a piecewise-defined control sequence [64]. Within each time interval $[t_{l-1}, t_l]$, a control operation P_l is applied. The operators Q_l represent the control propagators evaluated at the beginning of the l-th pulse, for $l = 1, 2, \ldots, n$.

In [64], the author uses the method of control matrix to analytically derive the expression of the filter function for a piecewise-defined control sequence. For each time-interval $[t_{l-1}, t_l]$, the corresponding control matrix is influenced by the control operation P_l and the cumulative control operator Q_l. For some complex composite pulse sequences, deriving the analytical form of the filter function using this method is complicated. In this section, we propose an simpler method, in which we numerically calculates the filter function. We illustrate our new method by calculating the filter function with respect to the SCROFULOUS composite pulse scheme.

As mentioned in Section 5.1, the SCROFULOUS composite pulse sequence Eq 4.21: $e^{-i\zeta\sigma_z\sigma_z}e^{i\frac{\theta}{2}I\sigma_x}e^{-i\frac{\pi}{2}\sigma_z\sigma_z}e^{-i\frac{\theta}{2}I\sigma_x}e^{-i\zeta\sigma_z\sigma_z}$, can be viewed as a three-process operation. For the first process which corresponds to the realization of the $e^{-i\zeta\sigma_z\sigma_z}$, we can simply follow the steps introduced in Section 6.1 to calculate its filter function F_{zz1}. Therefore, the F_{zz1} is given by:

$$F_{zz1}(f) = \frac{1}{\tilde{\delta\beta}} \int_0^{t_1} \tilde{H}_e^{int}(f, \tau)\, d\tau, \tag{6.17}$$

where the $\tilde{H}_e^{int}(f, \tau) = \tilde{\delta\beta} U^\dagger(t)(\sigma_z \otimes \sigma_z)U(t)$, and $U(t) = \exp\left(-iH^Q_{(1,1)}t\right)$. For the time renormalization required in the final expression of the filter function, we use the total

time duration.

We claim two important points that should be paid attention to when we calculate the filter function for this sequence. The first is that we need to stick to the same basis and qubit-frame when we do the calculation. This means the Hamiltonian we use to calculate the control unitary operator: $U_c(t)$ for the second process should also be the original $H^Q_{(1,1)}$. The reason is that the noise operator $\delta\beta(\sigma_z \otimes \sigma_z)$ maintains this form only in the same basis and frame. Therefore, when calculating the filter function, we can not treat the second process of this pulse sequence in another basis or frame.

This brings us to the second point: in the original basis and frame, the voltage pulse can be treated as implementing a single-qubit gate. We can see from Eq 4.30 that the g-tensor modulation is actually equivalent to $R_x(\theta)\vec{\sigma}_2$. Therefore, we can also consider the electric modulation of g-tensor as implementing a single qubit rotation around the X axes by rotation angle θ. This approach requires that the g-tensor modulation we perform to be very precise. As a result, for the second process, the effective Hamiltonian in the interaction picture is equal to:

$$\tilde{H}^{int}_{e2}(f,t) = \tilde{\delta\beta} U^\dagger(t_1) e^{i\frac{\theta}{2} I\sigma_x} U^\dagger(t)(\sigma_z \otimes \sigma_z) U(t) e^{-i\frac{\theta}{2} I\sigma_x} U(t_1). \tag{6.18}$$

The resulting filter function is given by:

$$F_{zz2}(f) = \frac{1}{\delta\beta} \int_{t_1}^{t_1+t_2} \tilde{H}^{int}_{e2}(f,\tau)\, d\tau. \tag{6.19}$$

In a similar way, for the third process, we just tune the voltages back to their original value, which is equivalent to implementing a reverse gate that rotates the second qubit around the X axis by an $-\theta$. The effective Hamiltonian and the filter function are as follows:

$$\tilde{H}^{int}_{e3}(f,t) = \tilde{\delta\beta} U^\dagger(t_1) e^{i\frac{\theta}{2} I\sigma_x} U^\dagger(t_2) e^{-i\frac{\theta}{2} I\sigma_x} U(t)(\sigma_z \otimes \sigma_z) U(t) e^{i\frac{\theta}{2} I\sigma_x} U(t_2) e^{-i\frac{\theta}{2} I\sigma_x} U(t_1), \tag{6.20}$$

$$F_{zz3}(f) = \frac{1}{\delta\beta} \int_{t_1+t_2}^{2t_1+t_2} \tilde{H}^{int}_{e3}(f,\tau)\, d\tau. \tag{6.21}$$

The total filter function is just the sum of these three functions, normalized by the total sequence duration:

$$F_{zz}(f) = \frac{1}{2t_1 + t_2} \left(F_{zz1}(f) + F_{zz2}(f) + F_{zz3}(f) \right). \tag{6.22}$$

Specifically, we are interested in the component: $F_{zz\otimes zz}(f)$, which is given by:

$$F_{zz\otimes zz}(f) = \frac{1}{4} Tr[F_{zz} \cdot (\sigma_z \otimes \sigma_z)]. \tag{6.23}$$

6.3. Results and discussion

Based on the procedures introduced in Section 6.1 and Section 6.2, we calculate the filter function $F_{zz\otimes zz}(f)$ for SCROFULOUS. As demonstrated in Fig 6.2(a), this filter function tends to zero when the frequency is approaching zero, which means it effectively suppresses the low-frequency component of the noise.

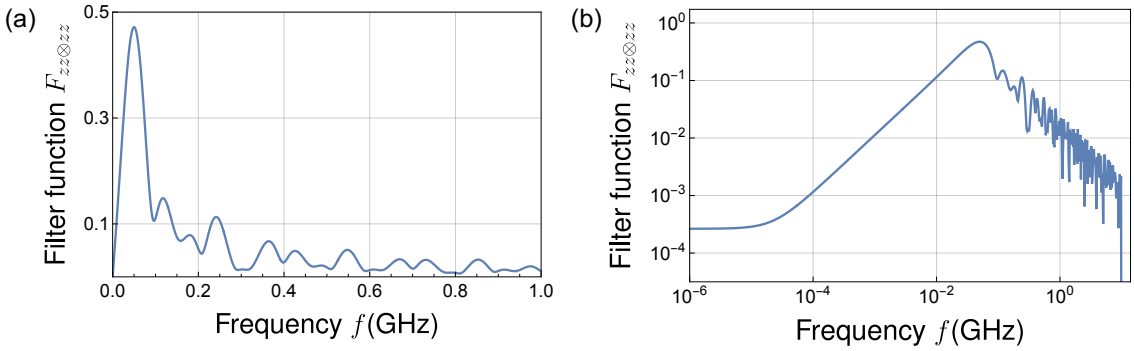

Figure 6.2: The filter function $F_{zz\otimes zz}(f)$ of the SCROFULOUS composite pulse sequence realized through hole spin qubits. (a) $F_{zz\otimes zz}(f)$ as a function of frequency. (b) $F_{zz\otimes zz}(f)$ plotted in the log-log scale.

Fig 6.2(b) focuses on the low-frequency region by employing a logarithmic scale on both the horizontal and vertical axes. We notice that as the frequency decreases to approximately 10^{-5}GHz, the filter function no longer follows a linear decline. This is caused by the disturbance term in the exchange coupling term $\vec{\sigma}_1 \cdot \mathcal{J}^{\mathcal{Q}}\vec{\sigma}_2$, which is only an approximate $\sigma_z \otimes \sigma_z$ operator in the rotating frame. We can confirm this by calculating the filter function using an ideal Hamiltonian:

$$H_{ideal} = \frac{1}{2}E_{z,1}\sigma_{z,1} + \frac{1}{2}E_{z,2}\sigma_{z,2} + \frac{1}{4}J^{Q}_{zz}\sigma_z\sigma_z. \tag{6.24}$$

The corresponding log-log scale filter function is given in Fig 6.3.

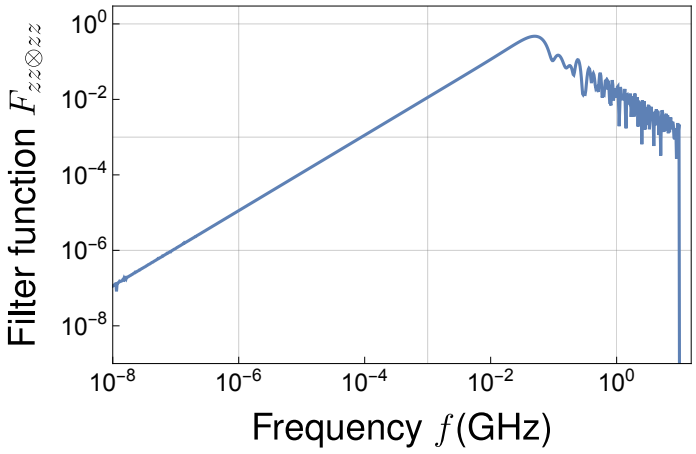

Figure 6.3: The filter function $F_{zz\otimes zz}(f)$ of the SCROFULOUS composite pulse sequence realized through a Hamiltonian with an ideal Ising-type exchange interaction.

We also calculated the filter function $F_{zz\otimes zz}(f)$ for the single-pulse ZZ gate and the adiabatic quantum gate introduced in Section 5.4. As demonstrated in Fig 6.4 and Fig 6.5, when the noise frequency approaches zero, both filter function values are approximately one, which means the adiabatic gate and the single-pulse ZZ gate is not robust to low-frequency noise in the $\sigma_z\sigma_z$. We notice that these two filter functions both drop to zero at multiples of $1/T$, where T is the duration time of one single gate operation. These points correspond to the cases in which the effect of the noise is equal to identity [66].

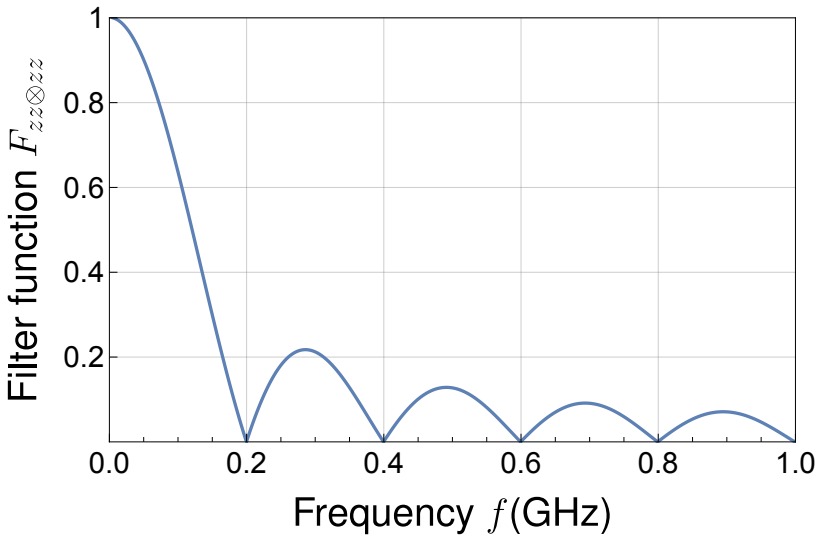

Figure 6.4: The filter function $F_{zz\otimes zz}(f)$ for the single-pulse ZZ gate.

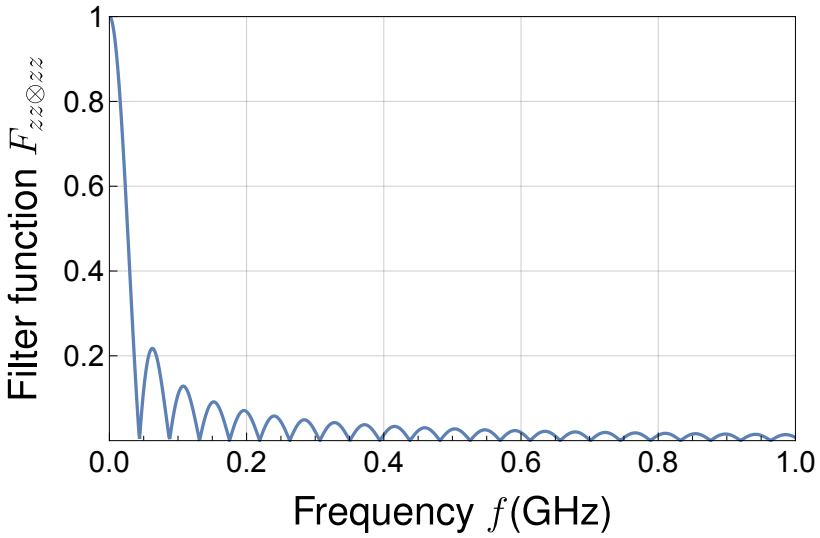

Figure 6.5: The filter function $F_{zz\otimes zz}(f)$ calculated through the adiabatic Hamiltonian: Eq 5.7.

Previously, we mentioned that we will use the filter function formalism to analyze the performance of SCROFULOUS and the single-pulse ZZ gate in the presence of the time-correlated and time-uncorrelated error we defined in Subsection 5.1.2. According

to Eq 6.9, the overlap between the power spectral density of the noise and the first-order filter function characterize the fidelity decay. Therefore, we first calculate the power spectral density of these two types of errors.

For the time-correlated error, its autocorrelation function is given by: $C(t_1, t_2) = \sigma^2$, where σ is the standard deviation of the Gaussian error. The power spectral density is defined as the Fourier transform of the autocorrelation function. Since the autocorrelation function is a constant, its Fourier transform results in a Dirac delta function: $\sigma^2\delta(f)$. Therefore, the power spectral density of the time-correlated error is a delta function centered at zero frequency. Comparing the filter function values of the SCROFULOUS, the single-pulse ZZ gate, and the adiabatic quantum gate at $f = 0$, we can clearly see that the SCROFULOUS's filter function approaches zero at $f = 0$, indicating small overlap. This means SCROFULOUS filters out a significant amount of low-frequency noise. In contrast, the filter functions of the single-pulse ZZ gate and the adiabatic ZZ gate are both close to 1 at $f = 0$, resulting in a much larger overlap, which can easily cause fidelity decay. This further confirms our conclusions in Subsection 5.1.2, where we demonstrated that in the presence of such time-correlated errors, SCROFULOUS performs much better than the single-pulse ZZ gate.

According to our definition of the filter function, the error is assumed to be weakly stationary: $C(t_1, t_2) = C(|t_1 - t_2|)$. However, the time-uncorrelated error defined in Subsection 5.1.2 does not actually satisfy this condition. Here, we relax the condition. Because the duration time of a single gate operation is short, we can approximate the error as a discrete sequence of independently sampled values, which makes it a kind of white noise. Specifically, the error is sampled from the Gaussian distribution $\mathcal{N}(0, \sigma^2)$ every interval T, and these sampled values are uncorrelated with each other. Therefore, the autocorrelation function is given by:

$$C(|t_1 - t_2|) = \begin{cases} \sigma^2, & |t_1 - t_2| = 0 \\ 0. & |t_1 - t_2| \neq 0 \end{cases} \tag{6.25}$$

We can also rewrite it using the Dirac delta function: $C(|t_1 - t_2|) = \sigma^2\delta(|t_1 - t_2|)$. The power spectral density is given by:

$$S(f) = \sigma^2. \tag{6.26}$$

The sampling theorem enables us to only focus on the frequency region: $(0, 1/T)$. We can see that the power spectral density of this error remains constant within this frequency region. It not only contains the zero-frequency component but also includes higher-frequency parts. Therefore, we observe that in this case, the filter function of SCROFULOUS also overlaps with the power spectral density of this error. This further supports our previous conclusion that SCROFULOUS is less effective in suppressing this type of error compared to time-uncorrelated ones. However, within a certain range, SCROFULOUS still exhibits some capability for error mitigation.

7

Conclusion and Future Research

7.1. Summary

In Chapter 2, we briefly introduced the necessary background knowledge for this thesis, focusing on some important concepts such as the exchange interaction between semiconductor quantum dot spin qubits, the physical background of hole spin qubits and the anisotropy induced by the spin-orbit interaction.

In Chapter 3, we introduced the basic concepts of composite pulse scheme, which is the core technique used in this project to construct noise-protected two-qubit gate. We showed two examples of composite pulse: SCROFULOUS and BB1. For single qubit gates constructed based on SCROFULOUS and BB1, they are robust against the pulse-length error; for corresponding two-qubit gates, they are robust against the J-tensor fractional error.

In Chapter 4, we studied the procedures to implement the SCROFULOUS composite pulse sequence by using two hole spin qubits in the germanium double quantum dot system. We first proposed the theoretical framework in which we explained how to transform the lab-frame Hamiltonian into the qubit-frame Hamiltonian. Based on that, we demonstrated how to realize a ZZ operator if the condition $|J_{zz}^{Q}|/|J_{\perp}| \gg 1$ is fulfilled. We further showed that the three operators in the middle can be viewed as one unified process which is achieved through electric modulation of g-tensor for quantum dot 2. We also discussed some points related to the practical implementation such as the phase compensation and synchronization and finally we showed the results and detailed simulation steps.

In Chapter 5, we designed some tests to analyze the robustness of this SCROFULOUS ZZ gate, under different types of noise:

- We started from modeling the J-tensor fractional error as a Gaussian-distribued error. We first calculated the expected process fidelity of SCROFULOUS and the single-pulse ZZ gate in the presence of the Gaussian error with different standard deviation. We found that the single-pulse ZZ gate showed a higher fidelity in the error-free case but its fidelity drops more rapidly than the SCROFULOUS

ZZ gate when the error's standard deviation increases. Then we simulated the cases in which we implemented the gates multiple times and further classified the error as time-correlated and time-uncorrelated based on its value during each gate operation. We found that SCROFULOUS shows an impressive robustness against the time-correlated error. Although its robustness against the time-uncorrelated error is less significant, SCROFULOUS still performs better than the single-pulse ZZ gate when the error and number of gates is not too large.

- Besides the J-tensor fractional error, we examine the impact of voltage fluctuations caused by charge noise. We first analyzed the influence of a fixed voltage fluctuation value on the performance of a single gate operation. We found that the average gate fidelity of SCROFULOUS drops rapidly compared with the single-pulse ZZ gate. We further assumed the voltage fluctuation follow a Gaussian distribution and calculated its approximate standard deviation. We did the similar simulation in which we implemented the gates consecutively multiple times with the time-correlated and time-uncorrelated error respectively. According to the simulation results, the SCROFULOUS ZZ gate performs worse than the single-pulse ZZ gate for both types of errors. We concluded that the SCROFULOUS is not robust against the phase errors introduced by voltage fluctuation.
- The SCROFULOUS ZZ gate protocol requires instant voltage changes on the electrostatic gates. If the voltage takes a certain amount of time to reach its preset value, this could also be a potential source of error. We examined a simple case: the ramp voltage pulse, in which the voltage value changes linearly within the transition time. We found that the gate's fidelity is very sensitive to the voltage transition time, which is mainly due to the phase errors accumulated.
- We finally compared the SCROFULOUS gate with an adiabatic ZZ gate. We calculated and compared the average gate fidelity for these two gates in the presence of both J-tensor fractional error and voltage fluctuations. Apart from obtaining conclusions similar to previous experiments, such as SCROFULOUS being more robust to J-tensor fractional errors but more sensitive to voltage fluctuations, we found that when both J-tensor fractional errors and voltage fluctuations are present, the SCROFULOUS ZZ gate exhibits higher fidelity if the voltage fluctuations are not too large.

In Chapter 6, we first introduced basic concepts of the filter function formalism and provided detailed steps to numerically calculate the filter function of the SCROFULOUS pulse sequence. We kept assuming the error term in the Hamiltonian takes the form: $\delta\beta e^{i2\pi ft}(\sigma_z \otimes \sigma_z)$ and calculated the filter function component: $F_{zz\otimes zz}(f)$ for the SCROFULOUS ZZ gate, the single-pulse ZZ gate, and the adiabatic ZZ gate. According to the plots, the filter function of SCROFULOUS remains close to zero as the frequency approaches zero. In contrast, for both the single-pulse ZZ gate and the adiabatic ZZ gate, the filter function takes a value of one at $f = 0$. This indicates that SCROFULOUS effectively filters out the low-frequency noise component, whereas the other two gate protocols do not. Furthermore, we computed the power spectral density of the time-correlated error and found that it takes the form of a delta function. Because the overlap between the SCROFULOUS filter function and this power spectral density

is minimal, SCROFULOUS effectively suppresses time-correlated errors. However, for the single-pulse ZZ gate and the adiabatic ZZ gate, the overlap is significantly larger, as their filter functions reach their maximum values at f = 0 . This explains why SCROFULOUS performs significantly better in suppressing time-correlated errors. For time-uncorrelated errors that approximate white noise, the power spectral density contains high-frequency components. Since the SCROFULOUS filter function also overlaps with these high-frequency components, its performance in mitigating time-uncorrelated errors is less effective compared to time-correlated errors.

7.2. Outlook

In this thesis, we only focused on the realization and analysis of a simple composite pulse sequence, the SCROFULOUS. However, it is worth noting that there exist some other more advanced composite pulse schemes that can not only eliminate the first-order error but also suppress higher-order errors. BB1, which we briefly introduced in Chapter 3, is one of the examples.

The ZZ gate implemented through BB1 composite pulse sequence shows a better robustness against the J-tensor fractional error. The trade-off is that its pulse sequence is much longer compared with SCROFULOUS. We need to perform two different basis transforms and apply the voltage pulses three times. This will lead to more phase errors and non-adiabatic errors that decrease the gate fidelity, which weakens its advantage. Therefore, exploring the suitable methods to implement the BB1 pulse sequence by using the hole spin qubit system represents a potential research direction.

Besides, as we have demonstrated in Section 5.2 and Section 5.3, the SCROFULOUS composite pulse sequence is vulnerable to the effect of charge noise and the phase errors induced by the voltage change time. The next steps should focus on exploring methods to mitigate or eliminate these effects. In order to suppress the voltage fluctuations induced by charge noise, apart from improving device design and materials, we can also try concatenated composite pulses [53]. These concatenated composite pulses incorporate two types of composite pulses such that they are robust against two types of errors simultaneously. Based on this idea, we can also design a concatenated composite pulse to make it robust against the J-tensor fractional error and phase errors simultaneously.

As for dealing with the problem of voltage transition time, we can explore ways to compensate for the phase errors it introduces. For example, based on the voltage transition time measured, we can find another voltage change set: $(\Delta V'_{B12}, \Delta V'_{B2}, \Delta V'_{P2})$ around the exact one. This second voltage change set should be specially designed such that the phase errors are compensated during the voltage transition process. After the voltage reaches the second voltage set, we then quickly tune it to the exact voltage set that is required to perform SCROFULOUS. This is only a preliminary idea, but it has the potential to address the errors introduced by voltage transition time.

8

Acknowledgements

How time flies! The completion of this thesis marks the end of my regular master study at TU Delft campus. During the past one and a half years, I gained a deeper understanding of quantum computing and I am very delighted to have the opportunity to apply what I have learned from books and lectures to practical research through this thesis project. Scientific research can never be done in isolation. From being a complete novice with little knowledge of semiconductor quantum dot spin qubits and quantum control to completing this fascinating project, this would not have been possible without the the support and guidance from many people and I would like to extend my gratitude to them here.

First and foremost, I would like to sincerely express my gratitude to my supervisor, Maximilian Rimbach-Russ. Max is patient, friendly and responsible towards students. During my master thesis project, I encountered many challenges and difficulties. It was Max's encouragement and support that helped me overcome them. I still remember that when I first started using Mathematica for calculations, due to the limited computational power of my laptop, I couldn't obtain satisfactory results. Setting up the server also took quite a bit of effort, and I felt rather frustrated about the progress I had made. At that time, Max encouraged me, comforting me that such challenges are something every researcher goes through. I really learned a lot from his words. What also touches me is that, despite Max's busy schedule every week, he is always very welcoming whenever I have questions to discuss. He always makes time to meet with me and guide me patiently through my problems. Besides, Max is incredibly knowledgeable. He has profound insights and expertise not only in the field of quantum computing but also in theoretical physics, algorithms, and more. This is something I deeply admire. I feel really lucky to have Max as my master thesis supervisor.

I also want to thank Christian and Yuning for their help and support. They both have a solid foundation in physics. Every time I had a discussion with them, I gained a lot of valuable insights. For example, the tips from Christian for my slides and presentation skills and the advice from Yuning for my Mathematica codes really help me a lot. In addition, I would also like to thank other friendly colleagues in Max's and Stefano's group: Edmondo, Tereza, Stefano, Michele and Minh. They gave me good advices

for my mock defense and I learned a lot from them during the weekly group meetings. It is my honor and fortune to be able to do research in such a positive and enthusiastic environment. They are all my role models, and in the future, I hope I can also become a PhD student like them.

I would also like to thank my friend Zhongyu. I really enjoy exchanging ideas on physics with him. Finally, I want to thank my parents for their unconditional support, not only financially but also in the choices I've made along my life journey, such as studying abroad and pursuing a degree in physics. I hope to live up to the efforts I've put in and continue pursuing a career I am passionate about in the future and one day have the opportunity to show my gratitude and care for my parents.

This research experience has profoundly influenced me and sparked my interest in semiconductor quantum dot spin qubits. My next research project will take me to the University of Basel, where I will continue exploring this fascinating field. At the same time, I plan to start applying for PhD positions, carrying forward my passion for scientific research. Years from now, when I look back on the projects and studies I have undertaken, I am certain this project will hold a special place in my memory. I will recall the sleepless nights spent debugging, the frustration and confusion of not understanding a paper, and the eventual moments of clarity and enlightenment when things finally made sense. Although this project has come to an end, it marks the beginning of my research journey.

Zizheng Wu
Delft, February 2025

A

Supplementary concepts / derivation

A.1. Average gate fidelity

Average gate fidelity is a widely used metric to quantify the performance of a quantum gate. Suppose the desired quantum gate is U and the actual quantum operation is $\mathcal{E}$, the average gate fidelity is given by:

$$F_{avg}(U,\mathcal{E}) = \int \mathrm{d}\psi \, \langle\psi|U^{\dagger}\mathcal{E}(|\psi\rangle\langle\psi|)U|\psi\rangle. \tag{A.1}$$

The $|\psi\rangle$ represents the pure states distributed uniformly over the Hilbert space (Haar measure) and it fulfills the condition: $\int \mathrm{d}\psi = 1$. This "average" ensures that the fidelity is not biased toward specific input states but reflects the gate's overall performance for the entire space of possible quantum states.

The expression can be reduced to a much more simplified version [68]:

$$F_{avg}(U,\mathcal{E}) = \frac{dF_p(U,\mathcal{E}) + 1}{d+1}, \tag{A.2}$$

where the $F_p(U,\mathcal{E})$ is another fidelity called process fidelity and d is the dimension of the quantum system. If our quantum gate is given by the corresponding time evolution operator $V(t)$ of Hamiltonian $H(t)$ which can be calculated through the Schrodinger equation:

$$i\hbar\dot{V}(t) = H(t)V(t), \tag{A.3}$$

$$V(0) = I, \tag{A.4}$$

and at some specific time point, we have the approximate quantum gate $\tilde{V}$, the process fidelity will be given by:

$$\frac{|tr(U^{\dagger}\tilde{V})|^2}{d^2}. \tag{A.5}$$

Plugging it into Eq A.2 and for the two-qubit system $d = 4$, we can finally arrive at a simple formula for calculating the average gate fidelity for two-qubit gates [29]:

$$F_{avg} = \frac{|tr(U^{\dagger}\tilde{V})|^2 + d}{d(d+1)} = \frac{|tr(U^{\dagger}\tilde{V})|^2 + 4}{20}. \tag{A.6}$$

A.2. Eigenenergies correspond to j=1/2 and 3/2

Squaring both sides of $\mathbf{j} = \mathbf{l} + \mathbf{s}$, we have $\mathbf{j}^2 = \mathbf{l}^2 + \mathbf{s}^2 + 2\mathbf{j}\cdot\mathbf{s}$. This enables us to rewrite the spin-orbit coupling term $\xi_{so}\mathbf{l}\cdot\mathbf{s} = \frac{\xi_{so}}{2}(\mathbf{j}^2 - \mathbf{l}^2 - \mathbf{s}^2)$. According to quantum mechanics, the eigenvalues of $\mathbf{j}^2$, $\mathbf{l}^2$ and $\mathbf{s}^2$ should be equal to [45]:

$$\mathbf{j}^2|\psi\rangle = \hbar^2 j(j+1)|\psi\rangle, \tag{A.7}$$

$$\mathbf{l}^2|\psi\rangle = \hbar^2 l(l+1)|\psi\rangle, \tag{A.8}$$

$$\mathbf{s}^2|\psi\rangle = \hbar^2 s(s+1)|\psi\rangle. \tag{A.9}$$

Therefore, the eigenvalues of $\xi_{so}\mathbf{l}\cdot\mathbf{s}$ are:

$$\hbar\xi_{so}[j(j+1) - l(l+1) - s(s+1)]. \tag{A.10}$$

For the valence band with a p-type orbital $l = 1$ and a spin-1/2 particle $s = 1/2$, j can choose between $3/2, 1/2$. Working in the unit of $\hbar = 1$ and plugging into $j = 3/2, l = 1, s = 1/2$ and $j = 1/2, l = 1, s = 1/2$ respectively, the two eigenergies are $\frac{\xi_{so}}{2}, -\xi_{so}$.

A.3. The rotating frame

Still working in the unit where $\hbar = 1$, the Hamiltonian of two coupled hole spins in the qubit frame is given by:

$$H^{Q}_{(1,1)} = \frac{1}{2}E_{z,1}\sigma_{z,1} + \frac{1}{2}E_{z,2}\sigma_{z,2} + \frac{1}{4}\vec{\sigma}_1 \cdot \mathcal{J}^{\mathcal{Q}}\vec{\sigma}_2. \tag{A.11}$$

Suppose the basis state is represented by $\psi\rangle$. It should satisfy the Schrodinger equation: $i\frac{d}{dt}|\psi\rangle = H^{Q}_{(1,1)}|\psi\rangle$. Let $|\tilde{\psi}\rangle = U^{\dagger}(t)|\psi\rangle$ which means we do a basis transform. Plugging $|\psi\rangle = U(t)|\tilde{\psi}\rangle$ into the Schrodinger equation, it becomes:

$$iU\frac{d}{dt}|\tilde{\psi}\rangle + i\left(\frac{d}{dt}U(t)\right)|\tilde{\psi}\rangle = H^{Q}_{(1,1)}U(t)|\tilde{\psi}\rangle. \tag{A.12}$$

Applying both sides with $U^\dagger(t)$ from the left side and rearranging the terms, the Schrodinger equation for the state $|\tilde{\psi}\rangle$ can be written as:

$$i\frac{d}{dt}|\tilde{\psi}\rangle = [U^\dagger(t)H^Q_{(1,1)}U(t) - iU^\dagger(t)\frac{d}{dt}U(t)]|\tilde{\psi}\rangle. \tag{A.13}$$

Therefore, the effective Hamiltonian $\tilde{H}$ in this basis can be expressed as:

$$\tilde{H} = U^\dagger(t)H^Q_{(1,1)}U(t) - iU^\dagger(t)\frac{d}{dt}U(t). \tag{A.14}$$

A.4. Rotation matrix in the decomposed g-tensor

$$R(\phi,\theta,\zeta) = \begin{pmatrix} \cos(\phi)\cos(\theta)\cos(\zeta) - \sin(\phi)\sin(\zeta) & -\sin(\phi)\cos(\zeta) - \cos(\phi)\cos(\theta)\sin(\zeta) & \cos(\phi)\sin(\theta) \\ \sin(\phi)\cos(\theta)\cos(\zeta) + \cos(\phi)\sin(\zeta) & \cos(\phi)\cos(\zeta) - \sin(\phi)\cos(\theta)\sin(\zeta) & \sin(\phi)\sin(\theta) \\ -\sin(\theta)\cos(\zeta) & \sin(\theta)\sin(\zeta) & \cos(\theta) \end{pmatrix} \tag{A.15}$$

A.5. Proof of $e^{-iUAU^\dagger} = Ue^{-iA}U^\dagger$

We can prove this by using the definition of the matrix exponential:

$$e^{-iX} = \sum_{n=0}^{\infty}\frac{(-iX)^n}{n!}, \tag{A.16}$$

The left-hand side can be written as:

$$e^{-iUAU^\dagger} = \sum_{n=0}^{\infty}\frac{(-i)^n(UAU^\dagger)^n}{n!}. \tag{A.17}$$

We can also write the right-hand side as:

$$Ue^{-iA}U^\dagger = U\left(\sum_{n=0}^{\infty}\frac{(-iA)^n}{n!}\right)U^\dagger = \sum_{n=0}^{\infty}U\frac{(-iA)^n}{n!}U^\dagger. \tag{A.18}$$

Using the property of unitary operators U, where $UU^\dagger = U^\dagger U = I$, we can show by induction that:

$$(UAU^\dagger)^n = UA^nU^\dagger. \tag{A.19}$$

Substituting this result into the left-hand side, we have:

$$e^{-iUAU^\dagger} = \sum_{n=0}^{\infty}\frac{(-i)^n(UAU^\dagger)^n}{n!} = \sum_{n=0}^{\infty}\frac{(-i)^nUA^nU^\dagger}{n!}. \tag{A.20}$$

For the right-hand side:

$$Ue^{-iA}U^\dagger = \sum_{n=0}^{\infty} U\frac{(-iA)^n}{n!}U^\dagger = \sum_{n=0}^{\infty}\frac{(-i)^n UA^nU^\dagger}{n!}. \tag{A.21}$$

Therefore, we can see that $e^{-iUAU^\dagger} = Ue^{-iA}U^\dagger$.

A.6. Dephasing time and voltage fluctuation

According to [58], the volatge change on the gates near the quantum dots will induce a variation of the g-tensor. Since the Zeeman term in the qubit-frame Hamiltonian is given by (using qubit 1 as an example):

$$H = \frac{1}{2}\mu_B R_1(g_1\vec{B})\cdot\vec{\sigma}_1 = \frac{1}{2}E_{z,1}\sigma_{z,1}, \tag{A.22}$$

we can see that the variation of the g-tensor will lead to the fluctuation of the Zeeman energy $E_{z,1}$. As a result, the Hamiltonian will be:

$$H = \frac{1}{2}((E_{z,0}+E_{z,1})\sigma_z), \tag{A.23}$$

where we assume the $E_{z,0}$ is the average energy and $E_{z,1}$ is the energy induced by the voltage fluctuation which follows a Gaussian distribution δv. For simplicity, we assume they follow a linear relation: $E_{z,1} = \alpha e\delta v$, where α is a constant and e is the elementary charge.

We can remove the average energy term in the rotating frame and the time evolution operator of this Hamiltonian becomes:

$$U(t) = e^{-i\frac{iE_{z,1}\sigma_z t}{2\hbar}} = \cos(\frac{E_{z,1}t}{2\hbar})I - i\sin((\frac{E_{z,1}t}{2\hbar}))\sigma_z. \tag{A.24}$$

Suppose now we want do a Ramsey experiment and prepare the state $|+\rangle = \frac{1}{\sqrt{2}}(|0\rangle + |1\rangle)$. We let the system evolve freely for time t and calculate the $|\langle +|U(t)|+\rangle|^2$, which equals to $\cos^2(\frac{E_{z,1}t}{2\hbar})$. Given that the voltage fluctuations follow a Gaussian distribution, their effect can be properly characterized by evaluating the following integral:

$$\int_{\infty}^{\infty}\cos^2(\frac{E_{z,1}t}{2\hbar})\cdot\frac{1}{\sqrt{2\pi}\sigma}e^{-\frac{(\delta v)^2}{2\sigma^2}}\,d\delta v. \tag{A.25}$$

Substituting $E_{z,1} = \alpha e\delta v$, its result will be $\frac{1}{2}(1+e^{-\frac{\alpha^2e^2\sigma^2t^2}{2\hbar^2}})$. At the initial time the value equals 1. When t increases, the value starts to decay and when it reaches $\frac{1}{2}(1+e^{-1})$, the corresponding time is T_2^*. Therefore, the expression for the T_2^* is $T_2^* = \frac{\sqrt{2}\hbar}{\alpha e\sigma}$.

B

Supplementary data

B.1. Data of g-tensor

The two g-tensors are derived from the g-tensor components given in [58].

$$g1 = \begin{pmatrix} 0.08288 & 0.01844 & 0.49529 \\ 0.01844 & 0.39412 & 0.02021 \\ 0.49529 & 0.02021 & 11.23300 \end{pmatrix}$$

$$g2 = \begin{pmatrix} 0.06538 & 0.00601 & 0.21444 \\ 0.00601 & 0.35958 & -0.03803 \\ 0.21444 & -0.03803 & 10.94564 \end{pmatrix}$$

B.2. Voltage-induced g-tensor variation

Table B.1: Description of $\frac{\partial \vec{g}}{\partial V_i}$ of Q2 for a voltage pulse applied to gates P2, B2, and B12 [58].

$\frac{\partial \vec{g}}{\partial V_i}$	P2	B2	B12
$\frac{\partial \phi}{\partial V_i}$ (mrad· mV^{-1})	-0.11(2)	1.3(2)	-3.1(1)
$\frac{\partial \theta}{\partial V_i}$ (mrad· mV^{-1})	0.0008(5)	0.005(4)	0.028(3)
$\frac{\partial \zeta}{\partial V_i}$ (mrad· mV^{-1})	0.04(2)	-2.3(1)	2.2(1)
$\frac{\partial g_{x'}}{\partial V_i}$ (mV^{-1})	0.000181(9)	-0.00028(7)	-0.00073(6)
$\frac{\partial g_{y'}}{\partial V_i}$ (mV^{-1})	0.000507(3)	0.00037(2)	-0.00146(2)
$\frac{\partial g_{z'}}{\partial V_i}$ (mV^{-1})	0.0045(1)	-0.0001(8)	-0.0071(7)

References

[1] Herman H Goldstine and Adele Goldstine. “The electronic numerical integrator and computer (ENIAC)”. In: *IEEE Annals of the History of Computing* 18.1 (1996), pp. 10–16.

[2] Jack S Kilby. “Turning Potential into Realities: The Invention of the Integrated Circuit.” In: *International Journal of Modern Physics B: Condensed Matter Physics; Statistical Physics; Applied Physics* 16.5 (2002).

[3] Suhas Kumar. “Fundamental limits to Moore’s law”. In: *arXiv preprint arXiv:1511.05956* (2015).

[4] Phillip Kaye, Raymond Laflamme, and Michele Mosca. *An introduction to quantum computing*. Oxford University Press, 2006.

[5] Philip Krantz et al. “A quantum engineer’s guide to superconducting qubits”. In: *Applied physics reviews* 6.2 (2019).

[6] Juan I Cirac and Peter Zoller. “Quantum computations with cold trapped ions”. In: *Physical review letters* 74.20 (1995), p. 4091.

[7] Emanuel Knill, Raymond Laflamme, and Gerald J Milburn. “A scheme for efficient quantum computation with linear optics”. In: *nature* 409.6816 (2001), pp. 46–52.

[8] Mark Saffman, Thad G Walker, and Klaus Mølmer. “Quantum information with Rydberg atoms”. In: *Reviews of modern physics* 82.3 (2010), pp. 2313–2363.

[9] Daniel Loss and David P DiVincenzo. “Quantum computation with quantum dots”. In: *Physical Review A* 57.1 (1998), p. 120.

[10] Guido Burkard et al. “Semiconductor spin qubits”. In: *Reviews of Modern Physics* 95.2 (2023), p. 025003.

[11] CH Yang et al. “Silicon qubit fidelities approaching incoherent noise limits via pulse engineering”. In: *Nature Electronics* 2.4 (2019), pp. 151–158.

[12] Xiao Xue et al. “Quantum logic with spin qubits crossing the surface code threshold”. In: *Nature* 601.7893 (2022), pp. 343–347.

[13] Tuomo Tanttu et al. “Assessment of the errors of high-fidelity two-qubit gates in silicon quantum dots”. In: *Nature Physics* (2024), pp. 1–6.

[14] Adam R Mills et al. “Two-qubit silicon quantum processor with operation fidelity exceeding 99%”. In: *Science Advances* 8.14 (2022), eabn5130.

[15] Mateusz T Mądzik et al. “Precision tomography of a three-qubit donor quantum processor in silicon”. In: *Nature* 601.7893 (2022), pp. 348–353.

[16] Akito Noiri et al. “Fast universal quantum gate above the fault-tolerance threshold in silicon”. In: *Nature* 601.7893 (2022), pp. 338–342.

[17] Kohei Itoh et al. “High purity isotopically enriched 70Ge and 74Ge single crystals: Isotope separation, growth, and properties”. In: *Journal of materials research* 8.6 (1993), pp. 1341–1347.

[18] Yinan Fang et al. “Recent advances in hole-spin qubits”. In: *Materials for Quantum Technology* 3.1 (2023), p. 012003.

[19] WIL Lawrie et al. “Simultaneous single-qubit driving of semiconductor spin qubits at the fault-tolerant threshold”. In: *Nature Communications* 14.1 (2023), p. 3617.

[20] Chien-An Wang et al. “Operating semiconductor quantum processors with hopping spins”. In: *Science* 385.6707 (2024), pp. 447–452.

[21] Valentin John et al. “A two-dimensional 10-qubit array in germanium with robust and localised qubit control”. In: *arXiv preprint arXiv:2412.16044* (2024).

[22] J. J. Sakurai. *Advanced Quantum Mechanics*. Addison-Wesley, 1967.

[23] Emmanuel I Rashba. “Spin dynamics and spin transport”. In: *Journal of superconductivity* 18 (2005), pp. 137–144.

[24] Christoph Kloeffel and Daniel Loss. “Prospects for spin-based quantum computing in quantum dots”. In: *Annu. Rev. Condens. Matter Phys.* 4.1 (2013), pp. 51–81.

[25] Bence Hetényi, Christoph Kloeffel, and Daniel Loss. “Exchange interaction of hole-spin qubits in double quantum dots in highly anisotropic semiconductors”. In: *Physical Review Research* 2.3 (2020), p. 033036.

[26] Jaime Saez-Mollejo et al. “Microwave driven singlet-triplet qubits enabled by site-dependent g-tensors”. In: *arXiv preprint arXiv:2408.03224* (2024).

[27] Simon Geyer et al. “Two-qubit logic with anisotropic exchange in a fin field-effect transistor”. In: *arXiv preprint arXiv:2212.02308* (2022).

[28] Maximilian Russ et al. “High-fidelity quantum gates in Si/SiGe double quantum dots”. In: *Physical Review B* 97.8 (2018), p. 085421.

[29] Maximilian Rimbach-Russ et al. “Simple framework for systematic high-fidelity gate operations”. In: *Quantum Science and Technology* 8.4 (2023), p. 045025.

[30] Benjamin CB Symons et al. “A practitioner’s guide to quantum algorithms for optimisation problems”. In: *Journal of Physics A: Mathematical and Theoretical* 56.45 (2023), p. 453001.

[31] Deepika Kumari et al. “Quantum Computing in Cryptography”. In: *2023 International Conference on Computational Science and Computational Intelligence (CSCI)*. IEEE. 2023, pp. 490–495.

[32] Weitang Li et al. “A hybrid quantum computing pipeline for real world drug discovery”. In: *Scientific Reports* 14.1 (2024), p. 16942.

[33] A Sedra et al. *Microelectronic circuits 8th edition*. Oxford University Press, 2020.

[34] C. Cohen-Tannoudji, B. Diu, and F. Laloë. *Quantum Mechanics, Volume 1: Basic Concepts, Tools, and Applications*. Wiley, 2019. ISBN: 9783527345533. URL: `https://books.google.nl/books?id=tVI_EAAAQBAJ`.

[35] Ronald De Wolf. “Quantum computing: Lecture notes”. In: *arXiv preprint* (2019).

[36] David P DiVincenzo. “The physical implementation of quantum computation”. In: *Fortschritte der Physik: Progress of Physics* 48.9-11 (2000), pp. 771–783.

[37] JM Elzerman et al. “Single-shot read-out of an individual electron spin in a quantum dot”. In: *nature* 430.6998 (2004), pp. 431–435.

[38] K Ono et al. “Current rectification by Pauli exclusion in a weakly coupled double quantum dot system”. In: *Science* 297.5585 (2002), pp. 1313–1317.

[39] Lieven MK Vandersypen and Mark A Eriksson. “Quantum computing with semiconductor spins”. In: *Physics Today* 72.8 (2019), pp. 38–45.

[40] Jason R Petta et al. “Coherent manipulation of coupled electron spins in semiconductor quantum dots”. In: *Science* 309.5744 (2005), pp. 2180–2184.

[41] Menno Veldhorst et al. “A two-qubit logic gate in silicon”. In: *Nature* 526.7573 (2015), pp. 410–414.

[42] David M Zajac et al. “Resonantly driven CNOT gate for electron spins”. In: *Science* 359.6374 (2018), pp. 439–442.

[43] Jonathan H Prechtel et al. “Decoupling a hole spin qubit from the nuclear spins”. In: *Nature materials* 15.9 (2016), pp. 981–986.

[44] Giordano Scappucci et al. “The germanium quantum information route”. In: *Nature Reviews Materials* 6.10 (2021), pp. 926–943.

[45] Eugen Merzbacher. *Quantum mechanics*. John Wiley & Sons, 1998.

[46] NW Hendrickx. “Qubit arrays in germanium”. In: (2021).

[47] Maximilian Rimbach-Russ et al. “A spinless spin qubit”. In: *arXiv preprint* arXiv:2412.13658 (2024).

[48] Biel Martinez et al. “Hole spin manipulation in inhomogeneous and nonseparable electric fields”. In: *Physical Review B* 106.23 (2022), p. 235426.

[49] Michael A Nielsen and Isaac L Chuang. *Quantum computation and quantum information*. Cambridge university press, 2010.

[50] Yuli V Nazarov and Jeroen Danon. *Advanced Quantum Mechanics: A Practical Guide*. Cambridge University Press, 2013.

[51] Lieven MK Vandersypen and Isaac L Chuang. “NMR techniques for quantum control and computation”. In: *Reviews of modern physics* 76.4 (2004), pp. 1037–1069.

[52] Frank Gaitan. *Quantum error correction and fault tolerant quantum computing*. CRC Press, 2008.

[53] Masamitsu Bando et al. “Concatenated composite pulses compensating simultaneous systematic errors”. In: *Journal of the Physical Society of Japan* 82.1 (2012), p. 014004.

[54] Holly K Cummins, Gavin Llewellyn, and Jonathan A Jones. “Tackling systematic errors in quantum logic gates with composite rotations”. In: *Physical Review A* 67.4 (2003), p. 042308.

[55] Tsubasa Ichikawa et al. “Minimal and robust composite two-qubit gates with Ising-type interaction”. In: *Physical Review A—Atomic, Molecular, and Optical Physics* 87.2 (2013), p. 022323.

[56] Utkan Güngördü and JP Kestner. “Pulse sequence designed for robust C-phase gates in SiMOS and Si/SiGe double quantum dots”. In: *Physical Review B* 98.16 (2018), p. 165301.

[57] Yu Tomita, JT Merrill, and Kenneth R Brown. “Multi-qubit compensation sequences”. In: *New Journal of Physics* 12.1 (2010), p. 015002.

[58] NW Hendrickx et al. “Sweet-spot operation of a germanium hole spin qubit with highly anisotropic noise sensitivity”. In: *Nature Materials* (2024), pp. 1–8.

[59] Simon Geyer et al. “Anisotropic exchange interaction of two hole-spin qubits”. In: *Nature Physics* (2024), pp. 1–6.

[60] Andreas Brinkmann. “Introduction to average Hamiltonian theory. I. Basics”. In: *Concepts in Magnetic Resonance Part A* 45.6 (2016), e21414.

[61] Harrison Ball, William D Oliver, and Michael J Biercuk. “The role of master clock stability in quantum information processing”. In: *npj Quantum Information* 2.1 (2016), pp. 1–8.

[62] Dimitrie Culcer, Xuedong Hu, and S Das Sarma. “Dephasing of Si spin qubits due to charge noise”. In: *Applied Physics Letters* 95.7 (2009).

[63] Tameem Albash and Daniel A Lidar. “Adiabatic quantum computation”. In: *Reviews of Modern Physics* 90.1 (2018), p. 015002.

[64] Todd J Green et al. “Arbitrary quantum control of qubits in the presence of universal noise”. In: *New Journal of Physics* 15.9 (2013), p. 095004.

[65] Łukasz Cywiński et al. “How to enhance dephasing time in superconducting qubits”. In: *Physical Review B—Condensed Matter and Materials Physics* 77.17 (2008), p. 174509.

[66] Ingvild Hansen et al. “Accessing the full capabilities of filter functions: Tool for detailed noise and quantum control susceptibility analysis”. In: *Physical Review A* 108.1 (2023), p. 012426.

[67] E Paladino et al. “1/f noise: Implications for solid-state quantum information”. In: *Reviews of Modern Physics* 86.2 (2014), pp. 361–418.

[68] Andrew G White et al. “Measuring two-qubit gates”. In: *Journal of the Optical Society of America B* 24.2 (2007), pp. 172–183.